The Astronomical Journal, 139:2504–2524, 2010 June doi:10.1088/0004-6256/139/6/2504

COMBINED ANALYSIS OF IMAGES AND SPECTRAL ENERGY DISTRIBUTIONS OF TAURUS PROTOSTARS

Luciana V. Gramajo[1], Barbara A. Whitney[2], Mercedes Gómez[1], and Thomas P. Robitaille[3,4]
[1] Observatorio Astronómico, Universidad Nacional de Córdoba, Laprida 854, 5000 Córdoba, Argentina; luciana@oac.uncor.edu, mercedes@oac.uncor.edu
[2] Space Science Institute, 4750 Walnut Street, Suite 205, Boulder, CO 80301, USA; bwhitney@spacescience.org
[3] Harvard-Smithsonian Center for Astrophysics, 60 Garden Street, Cambridge, MA 02138, USA; trobitaille@cfa.harvard.edu
Received 2009 June 18; accepted 2010 April 13; published 2010 May 4

ABSTRACT

We present an analysis of spectral energy distributions (SEDs), near- and mid-infrared images, and *Spitzer* spectra of eight embedded Class I/II objects in the Taurus–Auriga molecular cloud. The initial model for each source was chosen using the grid of young stellar objects (YSOs) and SED fitting tool of Robitaille et al. Then the models were refined using the radiative transfer code of Whitney et al. to fit both the spectra and the infrared images of these objects. In general, our models agree with previous published analyses. However, our combined models should provide more reliable determinations of the physical and geometrical parameters since they are derived from SEDs, including the *Spitzer* spectra, covering the complete spectral range; and high-resolution near-infrared and *Spitzer* IRAC images. The combination of SED and image modeling better constrains the different components (central source, disk, envelope) of the YSOs. Our derived luminosities are higher, on average, than previous estimates because we account for the viewing angles (usually nearly edge-on) of most of the sources. Our analysis suggests that the standard rotating collapsing protostar model with disks and bipolar cavities works well for the analyzed sample of objects in the Taurus molecular cloud.

Key words: circumstellar matter – infrared: stars – stars: formation – stars: imaging

Online-only material: color figures

1. INTRODUCTION

The Taurus–Auriga star-forming molecular cloud is a nearby region situated at a distance of 140 pc (Kenyon et al. 1994). Taurus-Auriga has a relatively low extinction (see, for example, Padoan et al. 2002), and the most dense cores form fairly isolated stars, unlike the Orion and the Ophiuchus regions (Motte & André 2001). The standard theoretical model describes a very similar situation as in the Taurus–Auriga cloud. This model suggests that a single low-mass star starts as a slow rotator similar to the dense cores. While the material with low angular momentum falls into the center of the protostar, the rest of the material forms a disk (Cassen & Moosman 1981). Early on in the infall process, the star–disk system starts to eject winds, primarily in the direction of the rotation axis (Belloche et al. 2002; Tafalla et al. 2004). These winds clear out the rotation axis zone of gas and dust, and produce jets and outflows. In a later phase, after the envelope has mostly collapsed to the disk or been dispersed by the outflows, the remaining disk material accretes slowly onto the central protostar. In general, the evolutionary process of the protostars can be divided in four classes (Class 0 to III) according to the shape of the spectral energy distribution (SED; Lada 1987; Adams et al. 1987; André et al. 1993). The Class 0 and I stages correspond to the initial envelope infall stage; Class II is the later disk accretion phase after the envelope has disperse; and Class III is the remnant or no-disk phase.

Models of the SEDs can provide information on the circumstellar material as well as constraints on the central source parameters. For example, the silicate feature near 10 μm is sensitive to the presence of small grains in the upper layers of the disk and to the inclination angle of the source (Furlan et al. 2008; Watson et al. 2004; Whitney et al. 2003b, hereafter W03b). The SED can put limits to the mass of the envelope, and the fluxes at millimeter wavelengths can constrain the mass of the disk. The modeling of (high-resolution) near- and mid-infrared images can provide information on the viewing angle, the extent and shape of the disk as well as the size and shape of the outflow cavity (Stark et al. 2006). Independent analyses of SEDs or images alone may not be sufficient to completely determine physical and geometrical parameters of Class I and II objects (Eisner et al. 2005). To achieve an accurate and comprehensive study of eight Taurus protostars, we performed a combined modeling of both the SED and the infrared images. To construct the SEDs we include 5–36 μm *Spitzer*/intensified Reticon spectrograph (IRS) spectra recently published by Furlan et al. (2008). This represents the most comprehensive modeling of these Taurus protostars to date.

We present the sample analyzed in Section 2, and in Section 3 we briefly describe the adopted model and outline the procedure employed in the combined analysis of SEDs and images. In Section 4, the individual source analysis is described. Finally, in Section 5, we summarize the results and present our conclusions.

2. THE SAMPLE

Our sample is composed of eight Class I/II sources belonging to the Taurus molecular cloud. We chose objects with *Hubble Space Telescope* (*HST*)/NICMOS and/or *Spitzer*/IRAC images, as well as detailed SEDs covering a wide spectral range. We included the 5–36 μm *Spitzer*/IRS spectra taken by Furlan et al. (2008). Table 1 shows the list of sources, the type of images available in each case, the SED-integrated luminosity calculated by Kenyon & Hartmann (1995), and the SED Class. *HST*/NICMOS images are from Padgett et al. (1999), whereas *Spitzer*/IRAC data are from the *Spitzer* Taurus Legacy Survey by Padgett et al. (2005). In particular, we analyzed the *HST*/NICMOS images obtained from the *HST* archive and reduced by Stark et al. (2006). *Spitzer*/IRAC images of Taurus stars in our sample were retrieved from the Spitzer Science Center Web

[4] Spitzer Postdoctoral Fellow.

Table 1
Selected Sample Observed with the *HST*/NICMOS[a] and *Spitzer*/IRAC[b]

Name	Telescope/Instrument	$L_{bol}(L_{\odot})$[c]	SED Class	Reference
IRAS 04016+2610	*HST*/NICMOS	3.70	I	1, 2
IRAS 04248+2612	*HST*/NICMOS	0.36	I	2, 3
	Spitzer/IRAC	0.34		
IRAS 04302+2247	*HST*/NICMOS	0.70	I	2
IRAS 04325+2402	*Spitzer*/IRAC	2.90	I	1
IRAS 04361+2547	*Spitzer*/IRAC	2.90	I	1
IRAS 04368+2557	*Spitzer*/IRAC	1.30	0/I	4
CoKu Tau 1	*HST*/NICMOS	0.29		
DG Tau B	*HST*/NICMOS	0.02	I/II	3

Notes.
[a] Padgett et al. (1999).
[b] Padgett et al. (2005).
[c] From Kenyon & Hartmann (1995).
References. (1) Duchene et al. 2004; (2) Kenyon & Hartmann 1995; (3) Hartmann et al. 2005; (4) André et al. 2000.

site[5] and processed using the GLIMPSE pipeline.[6] To construct the SEDs we compiled fluxes from the literature between 0.55 and 1300 μm, when available. *Spitzer*/IRS spectra were digitized from the Furlan et al. (2008) paper using the SpecScan[7] tool. Table 2 lists the specific fluxes used in each individual SED. For some sources, multiple flux values at the same wavelength are available in the literature. In general, we adopted an average value to fit the SED. However, in some cases we chose specified flux values to model. In Section 4, we indicate when this is the case. The uncertainties for the fluxes are not always available in the literature. In those cases we adopted "typical" errors.

3. ANALYSIS

As a starting model of each source, we used the SED fitting tool of Robitaille et al. (2007). This tool selects SEDs fit within a chosen χ^2 from a large grid of young stellar object (YSO) models[8] (Robitaille et al. 2006, hereafter R06). The grid consists of 20,000 radiation transfer models (Whitney et al. 2003b) of axisymmetric YSOs viewed at ten angles, resulting in a total of 200,000 SEDs, with a wavelength range of 0.36–1000 μm.

The 14 radiative transfer model parameters can be divided into three groups; the central source parameters: stellar mass (M_{star}), radius (R_{star}), and temperature (T_{star}); the infalling envelope parameters: envelope accretion rate ($\dot{M}$), envelope outer radius (R_{max}), cavity density (ρ_{cav}), cavity opening angle (θ, measured from the rotation axis at the outer radius of the envelope); and the disk parameters: disk mass (M_{disk}), disk outer (or centrifugal R_c) and inner radii (R_{min}), disk accretion rate ($\dot{M}_{disk}$), disk radial density exponent (A), disk scale height exponent (B), and the disk fiducial scale height (z_{01}, the scale height at R_{star} in units of R_{star}). The ambient density surrounding the young star (ρ_{amb}) is included as the 15th parameter.

In our analysis, we adopted "typical" ranges for the cavity density (ρ_{cav}) and the ambient density (ρ_{amb}) as in R06. Specifically 1×10^{-22}–8×10^{-20} g cm^{-3} for ρ_{cav} and 1.67×10^{-22}–6.68×10^{-22} ($M_{star}/M_{\odot}$) g cm^{-3} for ρ_{amb}. The fiducial scale height (z_{01}) was varied between 0.01 R_{star} and 0.03 R_{star} in our modeling. Finally, the inclination angle to the line of sight (i) is the 16th parameter of the model. Different parameters affect the SED (and can thus be constrained), depending on the evolutionary stage and wavelength range of the source. During the envelope infall stage (Class I), it is mainly the envelope parameters that are well determined by the SED fitting: that is, the envelope infall rate and mass; while the disk parameters are less well constrained. Similarly, during the later disk stage (Class II), the disk parameters are more well determined. The advantage of SED fitting from a large grid of models over determining a single best fit is that we can determine which parameters are well determined and which are not. For example, if the SED fitter returns a wide range of values for a certain parameter, that parameter is not well constrained. The wavelength range of the data is another important discriminator for both evolutionary stage and disk/envelope mass (Akeson et al. 2002; Eisner et al. 2005; Robitaille et al. 2007). As we will show, several parameters are better constrained when high-resolution images are available to include in the modeling of each source. For example, *HST*/NICMOS images of IRAS 04302+2247 (see Figure 4, bottom left panel) show a larger disk in comparison to IRAS 04248+2612 (see Figure 3, middle left panel).

Some of the model parameters are degenerate with each other in SED-fitting. The main degeneracies for the disk are the fiducial scale height z_{01} and the flaring exponent B. A model with a larger z_{01} could have a lower B and give a similar image. However, the SED will be more sensitive to z_{01} because of the flux from the inner wall. For the envelope, the centrifugal radius R_c is somewhat degenerate with the infall rate, in that increasing one while decreasing the other can give a similar envelope optical depth and therefore a similar SED. In this case, high-resolution images help to break this degeneracy by better determining R_c. The inclination is degenerate with luminosity since more edge-on sources tend to be fainter. Again, high-resolution imagery helps to break this degeneracy. These examples illustrate how the combination of images and SEDs improves the parameter estimates.

The YSO grid covers a wide range of evolutionary stages and masses: from embedded protostars to optically thin-disk Class III objects, and stellar masses from 0.1 to 50 $M_{\odot}$. Stellar temperatures and radii are from the pre-main sequence evolutionary tracks of Bernasconi & Meader (1996). For the envelope bipolar cavity, R06 adopted a curved shape and computed different models corresponding to increasing opening

[5] http://ssc.Spitzer.caltech.edu/legacy/all.html
[6] http://www.astro.wisc.edu/glimpse/docs.html
[7] SpecScan is a utility program that generates numerical data from printed spectra. It was created by Constantinos E. Efstathiou and is available at http://www.chem.uoa.gr/misc/specscan.htm.
[8] The grid and fitter are available at http://caravan.astro.wisc.edu/protostars/.

Table 2
Fluxes versus λ Used to Construct the SEDs

λ (μm)	Fluxes [F_ν(Jy)]				References
	IRAS 04016+2610	IRAS 04248+2612	IRAS 04302+2247	IRAS 04325+2402	
0.55	2.42×10^{-5}				Kenyon et al. (1993a)
0.63	6.17×10^{-5}				Kenyon et al. (1993a)
0.79	1.00×10^{-4}				Kenyon et al. (1993a)
0.89	1.00×10^{-4}				Eisner et al. (2005)
0.90			5.00×10^{-5}		Wolf et al. (2003)
1.10	3.00×10^{-4}	6.00×10^{-3}	6.40×10^{-4}		Padgett et al. (1999)
1.10				9.30×10^{-5}	Hartmann et al. (1999)
1.10			1.60×10^{-3}		Wolf et al. (2003)
1.22	5.50×10^{-3}				Kenyon et al. (1993a)
1.25		1.00×10^{-2}			Myers et al. (1987)
1.60	9.58×10^{-3}	2.09×10^{-2}	6.61×10^{-3}		Padgett et al. (1999)
1.60				3.10×10^{-3}	Hartmann et al. (1999)
1.60			1.04×10^{-2}		Wolf et al. (2003)
1.63	2.63×10^{-2}				Whitney et al. (1997)
1.63	2.17×10^{-2}				Kenyon et al. (1993a)
1.63	2.33×10^{-2}			4.45×10^{-3}	Park & Kenyon (2002)
1.65			1.49×10^{-2}		Park & Kenyon (2002)
1.65		2.60×10^{-2}			Myers et al. (1987)
1.65				4.68×10^{-3}	Whitney et al. (1997)
1.87	2.14×10^{-2}	2.13×10^{-2}	1.02×10^{-2}		Padgett et al. (1999)
1.87			1.81×10^{-2}		Wolf et al. (2003)
2.05	4.16×10^{-2}	2.05×10^{-2}	1.13×10^{-2}		Padgett et al. (1999)
2.05			1.83×10^{-2}		Wolf et al. (2003)
2.05				1.44×10^{-2}	Hartmann et al. (1999)
2.19	1.05×10^{-1}			1.74×10^{-2}	Park & Kenyon (2002)
2.19			2.26×10^{-2}		Whitney et al. (1997)
2.20	1.30×10^{-1}	4.00×10^{-2}	3.00×10^{-2}		Tamura et al. (1991)
2.20		4.00×10^{-2}	2.50×10^{-2}		Padgett et al. (1999)
2.20			2.50×10^{-2}		Barsony & Kenyon (1992)
2.20		3.10×10^{-2}			Myers et al. (1987)
3.45		1.80×10^{-2}			Myers et al. (1987)
3.45	4.60×10^{-1}				Kenyon et al. (1993a)
3.60		6.60×10^{-2}			Hartmann et al. (2005)
3.60	9.10×10^{-1}				Robitaille et al. (2007)
4.50		6.73×10^{-2}			Hartmann et al. (2005)
4.50	1.45				Robitaille et al. (2007)
4.75	2.05				Kenyon et al. (1993a)
5.80		7.89×10^{-2}			Hartmann et al. (2005)
5.80	1.71				Robitaille et al. (2007)
7.80	2.80				Myers et al. (1987)
8.00		1.12×10^{-1}			Hartmann et al. (2005)
8.69	2.10				Myers et al. (1987)
9.50	1.70				Myers et al. (1987)
10.00		2.20×10^{-1}			Kessler-Silacci et al. (2004)
10.30	2.50				Myers et al. (1987)
10.43		2.00×10^{-1}			Kessler-Silacci et al. (2004)
10.60	2.57				Kenyon et al. (1993a)
10.70	2.80	2.30×10^{-1}		6.00×10^{-2}	Kessler-Silacci et al. (2004)
11.60	3.40				Myers et al. (1987)
12.00	4.40	3.00×10^{-1}			Beichman et al. (1986)
12.00				$<2.50 \times 10^{-1}$	IRAS Point Source Catalog
12.00				4.00×10^{-2}	Clark (1991)
12.50	4.90				Myers et al. (1987)
17.90	4.57				Eisner et al. (2005)
21.00	$1.06 \times 10^{+1}$				Kenyon et al. (1993a)
25.00	$1.72 \times 10^{+1}$	1.60			Beichman et al. (1986)
25.00				2.10	IRAS Point Source Catalog
25.00			3.91×10^{-1}	2.26	Clark (1991)
60.00	$5.00 \times 10^{+1}$	4.70			Beichman et al. (1986)
60.00				1.29	IRAS Point Source Catalog
60.00			6.64	1.39	Clark (1991)
100.00	$6.23 \times 10^{+1}$				Kenyon et al. (1993a)
100.00			9.43	$2.50 \times 10^{+1}$	Clark (1991)
100.00	$5.57 \times 10^{+1}$			$2.24 \times 10^{+1}$	Barsony & Kenyon (1992)

Table 2
(Continued)

λ (μm)	Fluxes [F_ν(Jy)]				References
	IRAS 04016+2610	IRAS 04248+2612	IRAS 04302+2247	IRAS 04325+2402	
100.00	$5.40 \times 10^{+1}$	9.00			Beichman et al. (1986)
160.00	$4.66 \times 10^{+1}$				Kenyon et al. (1993a)
350.00	4.77				Kenyon et al. (1993a)
350.00	$1.25 \times 10^{+1}$	1.18	2.87		Andrews & Williams (2005)
450.00	4.23	2.96	1.88		Young et al. (2003)
450.00				6.06×10^{-1}	Andrews & Williams (2005)
450.00	2.82			3.60×10^{-1}	Hogerheijde & Sandell (2000)
450.00	3.29				Barsony & Kenyon (1992)
800.00	5.82×10^{-1}	2.52×10^{-1}	3.42×10^{-1}	3.01×10^{-1}	Moriarty-Schieven et al. (1994)
800.00	3.14×10^{-1}	1.20×10^{-1}		1.70×10^{-1}	Barsony & Kenyon (1992)
850.00	5.90×10^{-1}	5.60×10^{-1}	6.20×10^{-1}		Young et al. (2003)
850.00	1.92				Young et al. (2003)
850.00	4.30×10^{-1}			1.80×10^{-1}	Hogerheijde & Sandell (2000)
850.00				1.86×10^{-1}	Andrews & Williams (2005)
1100.00	5.32×10^{-1}	1.00×10^{-1}		2.30×10^{-2}	Barsony & Kenyon (1992)
1100.00	1.80×10^{-1}	9.90×10^{-2}	1.49×10^{-1}	7.40×10^{-2}	Moriarty-Schieven et al. (1994)
1100.00		1.50×10^{-2}			Dent et al. (1998)
1300.00	1.30×10^{-1}	6.00×10^{-2}	1.80×10^{-1}	1.10×10^{-1}	Andrews & Williams (2005)
1300.00	1.30×10^{-1}	6.00×10^{-2}	1.80×10^{-1}	1.10×10^{-1}	Motte & André (2001)
1300.00	5.80×10^{-2}				Eisner et al. (2005)
0.55			7.00×10^{-5}		Kenyon & Hartmann (1995)
1.22		1.80×10^{-3}			Kenyon et al. (1993a)
1.25		5.10×10^{-3}		1.95×10^{-3}	Robitaille et al. (2007)
1.25	6.40×10^{-4}		1.26×10^{-2}		Kenyon & Hartmann (1995)
1.63		3.50×10^{-3}			Kenyon et al. (1993a)
1.63	8.25×10^{-3}				Park & Kenyon (2002)
1.65	6.97×10^{-3}		2.56×10^{-2}		Kenyon & Hartmann (1995)
1.65	1.05×10^{-2}				Whitney et al. (1997)
1.66		3.11×10^{-2}		5.91×10^{-3}	Robitaille et al. (2007)
2.16		7.54×10^{-2}		1.42×10^{-2}	Robitaille et al. (2007)
2.16		5.94×10^{-4}			Tobin et al. (2008)
2.19	4.09×10^{-2}				Park & Kenyon (2002)
2.19					Whitney et al. (1997)
2.19		9.60×10^{-3}			Kenyon et al. (1993a)
2.19	3.75×10^{-2}		2.84×10^{-2}		Kenyon & Hartmann (1995)
2.20	4.00×10^{-2}				Tamura et al. (1991)
2.20					Padgett et al. (1999)
2.20	2.91×10^{-2}	3.80×10^{-3}			Whitney et al. (1997)
2.20	4.00×10^{-2}				Barsony & Kenyon (1992)
3.60		1.66×10^{-2}	2.17×10^{-2}		Hartmann et al. (2005)
3.60	2.65×10^{-1}			9.06×10^{-2}	Robitaille et al. (2007)
3.60		6.94×10^{-3}			Tobin et al. (2008)
4.50		1.72×10^{-2}	4.96×10^{-2}	2.88×10^{-1}	Hartmann et al. (2005)
4.50	3.54×10^{-1}				Robitaille et al. (2007)
4.50		2.28×10^{-2}			Tobin et al. (2008)
4.75					Kenyon et al. (1993a)
5.80		1.06×10^{-2}	1.03×10^{-1}	5.72×10^{-1}	Hartmann et al. (2005)
5.80	4.15×10^{-1}				Robitaille et al. (2007)
5.80		2.99×10^{-2}			Tobin et al. (2008)
6.70		2.24×10^{-2}			Tobin et al. (2008)
7.80					Myers et al. (1987)
8.00		6.10×10^{-2}	3.16×10^{-1}	8.30×10^{-1}	Hartmann et al. (2005)
8.00	8.81×10^{-1}				Robitaille et al. (2007)
8.00		1.88×10^{-2}			Tobin et al. (2008)
12.00				9.0×10^{-1}	Cohen & Schwartz (1987)
12.00			1.18		Weaver & Jones (1992)
12.00		$<2.50 \times 10^{-1}$			IRAS Point Source Catalog
12.00	2.12				Clark (1991)
12.00	1.66				Kenyon et al. (1994)
24.00			3.53		Robitaille et al. (2007)
25.00				3.7	Cohen & Schwartz (1987)
25.00			2.74		Weaver & Jones (1992)
25.00		7.00×10^{-1}			Benson & Myers (1989)
25.00		7.40×10^{-1}			IRAS Point Source Catalog

Table 2
(Continued)

λ (μm)	Fluxes [F_ν(Jy)]				References
	IRAS 04016+2610	IRAS 04248+2612	IRAS 04302+2247	IRAS 04325+2402	
25.00	$2.17 \times 10^{+1}$				Clark (1991)
25.00		6.94×10^{-1}			Kenyon et al. (1993a)
25.00	$1.89 \times 10^{+1}$				Kenyon et al. (1994)
60.00				$<3.66 \times 10^{+1}$	IRAS Faint Source Catalog
60.00			7.97		Weaver & Jones (1992)
60.00		$1.80 \times 10^{+1}$			Benson & Myers (1989)
60.00		$1.78 \times 10^{+1}$			IRAS Point Source Catalog
60.00	$5.00 \times 10^{+1}$		6.64		Clark (1991)
60.00		$1.74 \times 10^{+1}$			Kenyon et al. (1993a)
60.00	$4.18 \times 10^{+1}$				Kenyon et al. (1994)
100.00				$<4.76 \times 10^{+1}$	IRAS Faint Source Catalog
100.00	$4.30 \times 10^{+1}$		9.43		Clark (1991)
100.00	$4.44 \times 10^{+1}$				Kenyon et al. (1994)
100.00			$7.11 \times 10^{+1}$		Weaver & Jones (1992)
100.00		$7.20 \times 10^{+1}$			Benson & Myers (1989)
100.00		$7.13 \times 10^{+1}$			Kenyon et al. (1993a)
160.00		$6.88 \times 10^{+1}$			Kenyon et al. (1993a)
350.00		$1.20 \times 10^{+1}$			Kenyon et al. (1993a)
350.00				<5.17	Andrews & Williams (2005)
450.00	1.30	2.85	5.22×10^{-1}	<3.95	Andrews & Williams (2005)
450.00		3.21			Kenyon et al. (1993a)
800.00	6.34×10^{-1}				Moriarty-Schieven et al. (1994)
800.00		4.97×10^{-1}			Kenyon et al. (1993a)
850.00	1.21				Young et al. (2003)
850.00	2.75×10^{-1}	8.95×10^{-1}	3.50×10^{-2}	<1.10	Andrews & Williams (2005)
1100.00	1.88×10^{-1}				Moriarty-Schieven et al. (1994)
1300.00	1.10×10^{-1}		1.20×10^{-2}	$<7.00 \times 10^{-1}$	Andrews & Williams (2005)
1300.00		3.50×10^{-1}			Sarceno et al. (1996)
1300.00	3.40×10^{-1}	3.75×10^{-1}			Motte & André (2001)

Note. <: with this symbol we denote upper limit.

angles up to 60°. Similarly, for the rest of the parameters the grid fully spans all physical values for young stars, derived from theory and observations.

To model *HST*/NICMOS and/or *Spitzer*/IRAC images of the selected sources we used the Whitney et al. (2003a, hereafter W03a) code.[9] We initially used as input the set of parameter values corresponding to the best-fit SED derived from the R06 models. This initial set is based on the best fit of the SED, not including the *Spitzer* IRS spectrum, as R06's grid only admits flux values at specific wavelengths. We then produced a set of model images with W03b's code and re-ran it several times, refining the parameters to better reproduce both the observed images and SED. In these refinements we also included the *Spitzer* mid-infrared spectra of these objects recently obtained by Furlan et al. (2008). The image fitting was done by eye. In all cases we derived good fits that likely correspond to minima in χ^2. This by-eye approach was recently applied by Furlan et al. (2008) and Tobin et al. (2008) to find the best SED models for the objects they analyzed. For most of the objects in our sample (see Table 1), the combined SED+images modeling allows us to use all available information to better constraint physical and geometrical parameters of the star+envelope+disk system and derive a reliable configuration for each protostar. However, as we show in Section 4.5, for one of the stars (IRAS 04361+2546) the set of parameters derived from the SED+images analysis differs from the set that best fits the mid-infrared spectrum. In addition for DG Tau B (Section 4.8) we derive two models. The first reproduces the NICMOS images and the SED (including the IRS spectrum) but fails to fit the SED, and in particular the IRS spectrum, between 13 and 36 μm. The second model ignores the NICMOS images and fits the SED including the complete IRS spectrum from 5 to 36 μm, but fails to fit fluxes for wavelengths shorter than 3 μm.

The SED has the advantage, as mentioned before, of the wide wavelength coverage, including the submillimeter region, which can determine envelope/disk masses, while high-resolution near-infrared images better constrain the viewing angle, disk size cavity shape and opening angle, and evolutionary stage. The mid-infrared data and, in particular, spectra in these wavelengths are useful to constraint the parameters of the disk such as the scale height factor, the flaring parameter, and the disk mass accretion rate. In addition, Class I sources usually show absorptions in the mid-infrared due to water ice and silicates (see, for example, Pontoppidan et al. 2003; Watson et al. 2004; Furlan et al. 2008). The modeling of these spectral features can help to better determine the set of physical and geometrical parameters for each star.

Table 3 shows the procedure applied to model both the SED (including the mid-infrared spectrum) and the images of IRAS 04248+2612. We initially used the R06 grid to model the SED. Note that we are simply looking for a starting point for the models so are using the lowest-χ^2 fit from the model grid. If we wished to better estimate the model parameters from the SED-fitting only, we would consider the range of well-fit models. Two of the best-fit models are shown as models 1 and 2

[9] Also available at http://caravan.astro.wisc.edu/protostars/.

Table 3
Different Models for IRAS 04248+2612

Parameter	Model 1[a]	Model 2[b]	Model 3[c]
$M_{\rm star}$ ($M_\odot$)	0.11	0.22	0.07
$R_{\rm star}$ ($R_\odot$)	2.56	2.33	0.9
$T_{\rm star}$ (K)	2768	3131	2845
$\dot{M}$ ($M_\odot$ yr^{-1}; envelope mass accretion rate)	1.9×10^{-5}	1.1×10^{-5}	4.39×10^{-6}
R_c (AU; centrifugal radius)	31.1	109.0	60.0
$R_{\rm min}$ ($R_{\rm star}$; inner disk radius)	36.1	54.2	3.7
$R_{\rm max}$ (AU; envelope outer radius)	1426	2122	9000
$M_{\rm disk}$ ($M_\odot$)	0.001	0.005	0.010
$\dot{M}_{\rm disk}$ ($M_\odot$ yr^{-1}; disk mass accretion rate)	2.5×10^{-11}	1.4×10^{-7}	1.0×10^{-8}
z_{01} (fiducial scale height)	0.033	0.014	0.010
A (disk radial density exponent)	2.120	2.135	2.280
B (disk scale height exponent)	1.120	1.135	1.280
θ(°; cavity opening angle[d])	13.6	14.5	16.0
i(°; inclination)	18.2	69.5	65.0

Notes. [a] First fit from the R06 grid with a $\chi^2 \sim 168$.
[b] Second fit from the R06 grid with a $\chi^2 \sim 214$.
[c] Combined SED+images fit.
[d] Measured from the rotation axis.

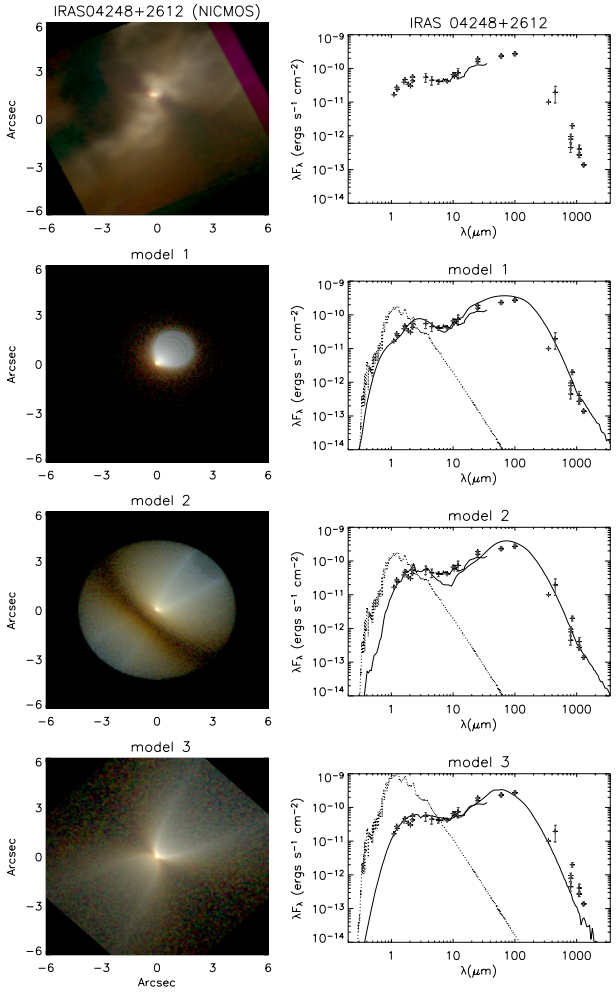

Figure 1. Illustration of the procedure applied to derive the best combined (SED+*Spitzer*/IRS spectrum+image) model for IRAS 04248+2612. The top panel shows the observed NICMOS images (north is up and east is to the left), and the SED, including the *Spitzer* IRS spectrum (Furlan et al. 2008). The second and the third panels (models 1 and 2) correspond to the first and second SED fits using the R06 grid (see Table 3). On the left side, we show the resultant model image calculated using the W03b code. Finally the bottom panel, model 3, shows the best combined SED+images models. The dotted line indicates the Kurucz model for the stellar photosphere.

(A color version of this figure is available in the online journal.)

in Table 3. Model 3 in this table corresponds to the best solution found for this object from fitting the images in addition to the SED.

Figure 1 (top panel) shows the observed NICMOS images and the SED, including Furlan et al.'s (2008) mid-IR spectrum. The source is nearly edge-on with a small flared disk that casts a shadow in the disk midplane (Stark et al. 2006). The middle panels show two SED fits derived from the R06 grid as well as the corresponding images, obtained by applying the W03b code (models 1 and 2 in Table 3). These initial SED models clearly have the wrong inclination (second panel) or disk size (third panel). Using W03b's code we varied the viewing angle and disk size accordingly to reproduce the images and SEDs.

Changing the viewing angle required adjusting the luminosity of the source (an edge-on view of a source will have less flux than a pole-on; W03a). Rescaling the luminosity, and estimating the stellar temperature (taken from spectroscopic determinations or fixed to a "typical" value, as explained below), we derive the stellar radius for each source. The luminosity and the stellar temperature in combination with the pre-main sequence evolutionary tracks of Siess et al. (2000) allow us to estimate the mass of the central star. We assumed solar metallicities for our sources and a "typical" age of $\sim 10^5$ yr, corresponding to the Class I stage. We used the radiation transfer code to refine this set of parameters (the stellar temperature and luminosity). In this manner, we searched for a common solution that provides a good match for both the SED (including the mid-infrared spectrum) and the images, as shown in the bottom panel of Figure 1. Table 3 lists this model as model 3.

Table 4 shows the initial result obtained with the R06 models for all of the sources in our sample (see Table 1). Table 5 lists the final combined (SED+images) models, and Figures 2–13 show the corresponding fits. In general, model SEDs in Figures 1–13 correspond to an aperture of 35″. The exceptions are IRAS 04016+2610 with an aperture of 60″ and IRAS 04368+2557 with two apertures of 8″ and 26″, as we discuss in Sections 4.1 and 4.6. Observed and model images are shown as three-color composite images: the *HST*/NICMOS *F110W*, *F160W*, and *F205W* images are displayed in blue, green, and red, respectively. Similarly, *Spitzer*/IRAC [3.6], [4.5], and [8.0] bands are shown in blue, green, and red. For

Table 4
Initial SED Results Derived Using the R06 Models

Object	M_{star} ($M_\odot$)	R_{star} ($R_\odot$)	T_{star} (K)	$\dot{M}$ ($M_\odot$ yr^{-1})	R_c (AU)	R_{min} (R_{star})	R_{max} (AU)	M_{env} ($M_\odot$)	M_{disk} ($M_\odot$)	$\dot{M}_{disk}$ ($M_\odot$ yr^{-1})	A	B	θ (°)	i (°)	L_{tot} ($L_\odot$)
IRAS 04016+2610	0.44	5.84	3615	4.8×10^{-6}	47.8	1.0	2530	0.07	0.004	1.2×10^{-07}	2.082	1.082	3.1	63.2	5.47
IRAS 04248+2612	0.22	2.33	3131	1.1×10^{-5}	109.0	54.2	2122	0.15	0.005	1.4×10^{-07}	2.135	1.135	14.5	69.5	0.47
IRAS 04302+2247	0.19	2.85	3024	2.8×10^{-5}	57.9	98.6	5786	0.31	0.001	4.4×10^{-09}	2.136	1.136	32.5	31.8	0.62
IRAS 04325+2402	0.41	3.17	3617	2.9×10^{-6}	68.9	159.4	4190	0.72	0.001	6.2×10^{-10}	2.178	1.178	32.9	69.5	1.54
IRAS 04361+2547	0.21	4.89	3092	5.6×10^{-6}	7.6	1.0	2368	0.10	0.001	1.1×10^{-07}	2.037	1.037	8.5	18.2	2.09
IRAS 04368+2557	0.13	4.05	2741	3.7×10^{-5}	9.5	136.2	2977	1.26	0.001	4.5×10^{-08}	2.209	1.209	7.1	18.2	0.87
CoKu Tau 1	1.27	4.15	4380	6.9×10^{-7}	105.5	23.8	6180	0.02	0.032	2.5×10^{-07}	2.009	1.002	39.9	87.1	7.60
DG Tau B	0.13	4.56	2706	1.0×10^{-6}	2.3	1.0	1569	0.11	0.003	1.1×10^{-07}	2.029	1.029	3.9	49.5	1.81

Note. Symbols for model parameters are as indicated in Table 3.

Table 5
Combined SED and Images Results for the Selected Sample

Object	M_{star} ($M_\odot$)	R_{star} ($R_\odot$)	T_{star} (K)	$\dot{M}$ ($M_\odot$ yr^{-1})	R_c (AU)	R_{min} (R_{star})	R_{max} (AU)	M_{env} ($M_\odot$)	M_{disk} ($M_\odot$)	$\dot{M}_{disk}$ ($M_\odot$ yr^{-1})	A	B	θ (°)	i (°)	L_{tot} ($L_\odot$)
IRAS 04016+2610	2.50	2.10	4580[a]	5.0×10^{-6}	120.0	10.0	5000	0.06	0.010	1.0×10^{-8}	2.300	1.300	20.0	50.0	4.51
IRAS 04248+2612	0.07	0.90	2845[a]	4.4×10^{-6}	60.0	11.7	9000	0.10	0.010	1.0×10^{-8}	2.280	1.280	16.0	65.0	1.05
IRAS 04302+2247	0.50	2.85	3800	9.0×10^{-6}	500.0	20.0	1870	0.12	0.070	5.4×10^{-10}	2.220	1.220	6.0	83.0	1.52
IRAS 04325+2402	0.41	3.17	3150	2.9×10^{-6}	68.9	661.1	3500	0.12	0.0001	6.2×10^{-10}	2.180	1.180	20.0	55.0	1.21
IRAS 04361+2547[b]	0.80	3.10	4100	1.3×10^{-6}	40.0	2.0	3600	0.02	0.001	1.1×10^{-7}	2.040	1.040	8.4	18.2	2.51
IRAS 04361+2547[c]	0.35	3.80	4100	4.2×10^{-6}	50.0	50.0	3600	0.02	0.001	1.1×10^{-7}	2.200	1.200	10.0	70.0	3.67
IRAS 04368+2557	0.70	3.00	4000	3.0×10^{-5}	250.0	7.0	5000	0.82	0.060	3.0×10^{-7}	2.250	1.250	30.0	80.0	3.98
CoKu Tau 1	0.70	3.50	4000[a]	1.4×10^{-7}	30.0	28.8	3600	0.003	0.003	2.4×10^{-8}	2.176	1.176	20.0	81.3	1.91
DG Tau B[d]	0.70	2.50	4000	8.0×10^{-6}	300.0	14.4	1157	0.03	0.100	5.0×10^{-7}	2.210	1.210	11.0	70.0	2.10
DG Tau B[e]	0.80	2.70	4100	3.8×10^{-6}	100.0	12.2	1157	0.03	0.060	8.0×10^{-7}	2.050	1.050	4.0	70.0	4.00

Notes. Symbols for model parameters are as indicated in Table 3.
[a] Temperature values were obtained from White & Hillenbrand (2004).
[b] IRAS 04361+2547, model a: parameters derived from the SED(without the IRS spectrum)+the images modeling (see Figure 8).
[c] IRAS 04361+2547, model b: parameters derived from the SED(excluding the IRAC fluxes)+the *Spitzer*/IRS spectrum+the images modeling (see Figure 9).
[d] DG Tau B, model a: parameters derived from the NICMOS images+SED, excluding the 12–36 μm region (see Figure 12).
[e] DG Tau B, model b: parameters derived from the SED, including the IRS spectrum, but ignoring the NICMOS images (see Figure 13).

the model images we matched both the pixel scale and the field of view of the observed images.

4. INDIVIDUAL SOURCE ANALYSIS

In this section, we present and discuss the analysis and results on each source.

4.1. IRAS 04016+2610

This source, also known as L1489 IRS, is a Class I object associated with a molecular outflow (Hogerheijde et al. 1998). However, Hogerheijde & Sandell (2000) suggested that IRAS 04016+2610 is in a transitional phase between the Class I and II stages. Gómez et al. (1997) found a pattern of optical knots surrounding IRAS 04016+2610 that suggest multiple cavities in the envelope. Lucas & Roche (1997) interpreted their near-infrared polarimetry images as arising from scattering in an envelope with orthogonal bipolar cavities. Wood et al. (2001) analyzed *I*-band and *HST* NICMOS *F160W* and *F205W* images and attributed the complex scattered light pattern shown by these images to presence of two sets of cavities in the infalling envelope.

The SED, shown in Figure 2, has a strong absorption feature at 10 μm. The 5–36 μm *Spitzer*/IRS spectrum of this source clearly delineates this feature (Furlan et al. 2008). Fluxes in the millimeter and submillimeter region are not as uniformly distributed as in the infrared wavelengths, which impose an extra difficulty when trying to model the SED. The scarcity of data in the millimeter and submillimeter region, however, is common to all the targets in our sample. On the other hand, *Spitzer*/IRS spectra provide well-defined SEDs in the mid-infrared.

In the NICMOS images observed by Padgett et al. (1999), IRAS 04016+2610 appears as a point source associated with a reflection nebula. They noted that the reflection nebula was crossed by a dark lane extended about 600 AU in the east–west orientation.

As an initial approximation we used the grid of models of R06 and derived a stellar temperature $T_{star} = 3615$ K, from this SED fitting tool. The corresponding set of parameters is given in Table 4. Robitaille et al. (2007) analyzed this source with the grid method allowing the stellar temperature to be a free parameter. They derived a range of solutions that in general comprises the model in Table 4. However we note a difference in the inclination angle (63.°2 versus 18°–41°).

We next carried out a combined SED (including the *Spitzer*/IRS spectrum) and NICMOS images modeling. We used the NICMOS images to constrain the inclination angle and varied the rest of the parameters to refine the initial solution give by the R06 models. In this modeling approach, we adopted for the stellar temperature the value ($T_{star} = 4580$ K) determined by White & Hillenbrand (2004) from an optical spectrum. Table 5 lists the final set of parameters. This result suggests that this

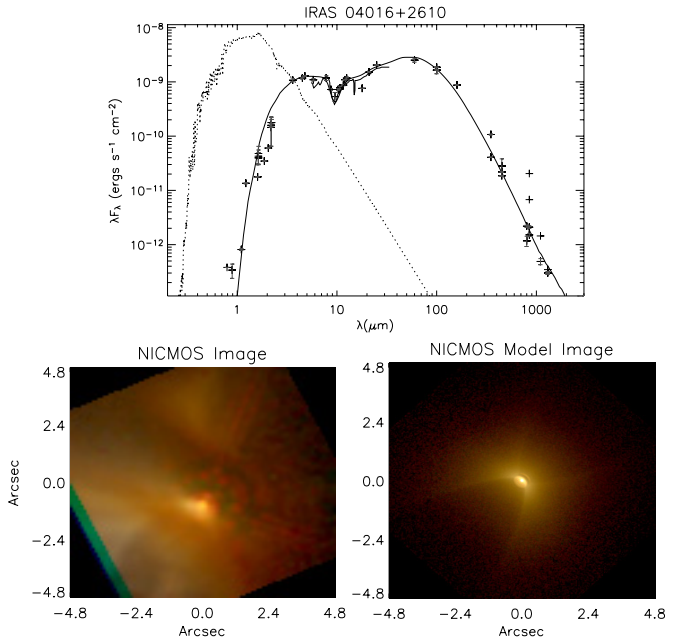

Figure 2. IRAS 04016+2610 combined (SED+images) model (Table 5). The upper panel displays the SED model for an aperture of 60″ (continuous line), the *Spitzer* 5–36 μm spectrum and the observed fluxes. The dotted line indicates the Kurucz model for the stellar photosphere. The bottom left panel shows the *HST*/NICMOS image (Padgett et al. 1999), where north is up and east is to the left. The bottom right panel corresponds to the best combined (SED+images) model image.

(A color version of this figure is available in the online journal.)

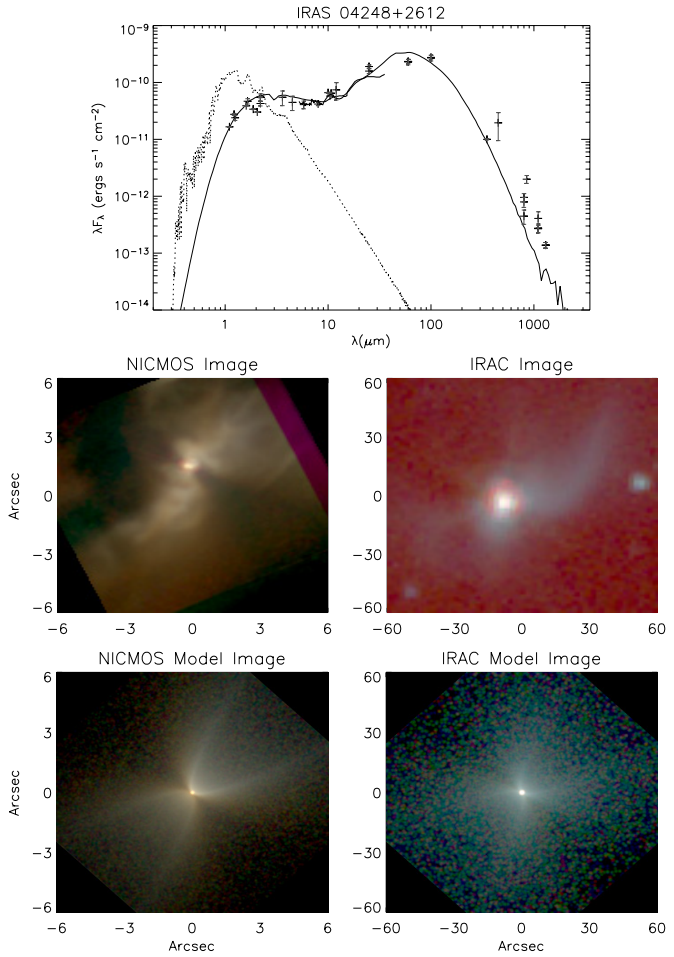

Figure 3. IRAS 04248+2612 combined (SED+images) model (see Table 5). The upper panel shows the best combined model SED, the *Spitzer* 5–36 μm spectrum, and the observed fluxes. The dotted line shows the Kurucz model for the stellar photosphere. The middle left panel shows the *HST*/NICMOS image (Padgett et al. 1999) and the middle right, the *Spitzer*/IRAC images (Padgett et al. 2005), where north is up and east is to the left. The bottom images display the best combined (SED+images) model corresponding to NICMOS and IRAC wavelengths.

(A color version of this figure is available in the online journal.)

object is a Class I source in agreement with Kenyon & Hartmann (1995) and Duchene et al. (2004). For this model we considered the orientation and appearance of the NICMOS images showing only one of the cavity lobes, suggesting an intermediate value for the inclination angle ($i \sim 50^\circ$). Our results basically coincide with those obtained by Stark et al. (2006), who modeled the *HST* NICMOS images.

We note that our best model in Table 5 reproduces well the 10 μm absorption feature, the 5–36 μm *Spitzer*/IRS spectrum and the *HST* images (see Figure 2). The fluxes around 2 and 1000 μm show a large dispersion and are of less significance when trying to fit the SED. The dispersion in the near-infrared region of the SED is probably due to the variability of this source (Park & Kenyon 2002). The model in Table 5 does not reproduce the observed flux at 17.9 μm (see Table 2). Eisner et al. (2005) suggested that this flux value could be affected by poor seeing conditions during the observations. The model SED plotted in Figure 2 corresponds to an aperture ∼60″. Around 850 μm the model overestimates the observed fluxes obtained with an aperture of ∼40″ (Young et al. 2003) and underestimates the fluxes measured with an aperture ∼120″. Clearly, the poor fit around 850 μm is due to an aperture effect. R06 found the same peculiarity in their model SED with respect to the observed SED.

Table 6 summarizes different models from the literature. For comparison purposes, we also include in Table 6 the models presented in Table 4, our grid model, and in Table 5, our combined (SED+ images) model. The inclusion of the NICMOS images in our models produces different values for some of the parameters with respect to the R06 grid, for example, the cavity opening angle (θ: 20° versus 3.°1). For the envelope mass accretion rate, the mass of the envelope and the inclination to the line of sight both approaches produce similar values ($\dot{M}$: $5 \times 10^{-6}\,M_\odot$ yr^{-1} versus $4.8 \times 10^{-6}\,M_\odot$ yr^{-1}; $M_{\rm env}$: $0.06\,M_\odot$ versus $0.07\,M_\odot$; i: 50° versus 63.°2).

Hogerheijde et al. (1998) observed an outflow in ^{12}CO 3–2 associated with this source and derived an inclination to the line of sight of $i = 60^\circ$ that roughly agrees with the value we derived ($i = 50^\circ$). Padgett et al. (1999), from the *HST*/NICMOS images, estimated a cavity opening angle of $\theta = 52.^\circ5$ at 1 μm and $\theta = 80.^\circ0$ at 2 μm. We derived an opening angle ($\theta = 20.^\circ0$) quite small in comparison with Padgett et al.'s (1999) determination. Part of this discrepancy is that our opening angle is defined at the envelope outer radius of 5000 AU, which is larger than where Padgett et al. (1999) measured it. We also note that this source likely has a three-dimensional geometry (see Wood et al. 2001), so our cavity size is just an approximation for an azimuthally symmetric model. From submillimeter observations, Andrews & Williams (2005) obtained a mass of the disk $M_{\rm disk} = 0.02\,M_\odot$. Ohashi et al. (1996) derived an upper limit for the disk mass of $M_{\rm disk} < 0.022\,M_\odot$, using 3 mm continuum observations as well as the CS line. Our determination agrees with these estimates ($M_{\rm disk} = 0.01\,M_\odot$). White & Hillenbrand (2004) derived a disk mass accretion rate $\dot{M}_{\rm acc} = 7.1 \times$

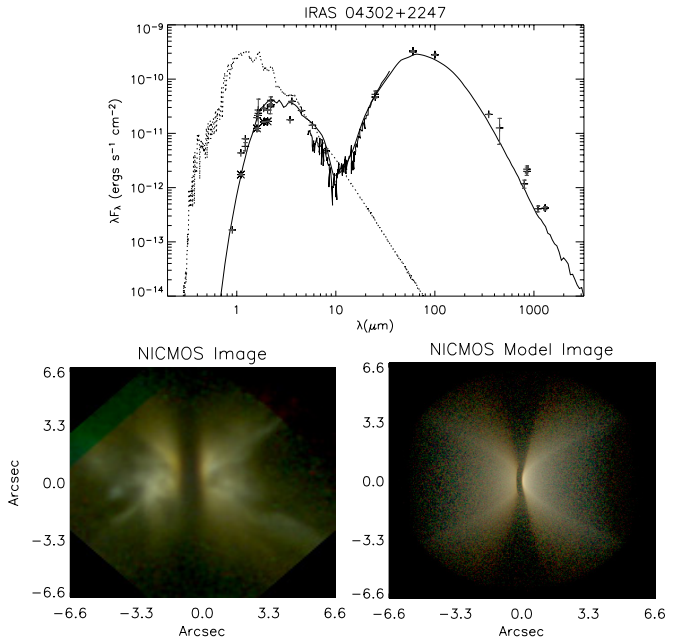

Figure 4. Model of the SED including the IRS spectrum but ignoring the NICMOS fluxes for IRAS 04302+2247 (model a in Table 8, left column). The upper panel displays the SED model, the *Spitzer* 5–36 μm spectrum and the observed fluxes, where the asterisks correspond to the NICMOS fluxes (Padgett et al. 1999) and the crosses to data published by other authors (see Table 2). The dotted line indicates the Kurucz model for the stellar photosphere. The bottom left panel shows the *HST*/NICMOS image (Padgett et al. 1999), where north is up and east is to the left. The bottom right panel displays the corresponding model image.

(A color version of this figure is available in the online journal.)

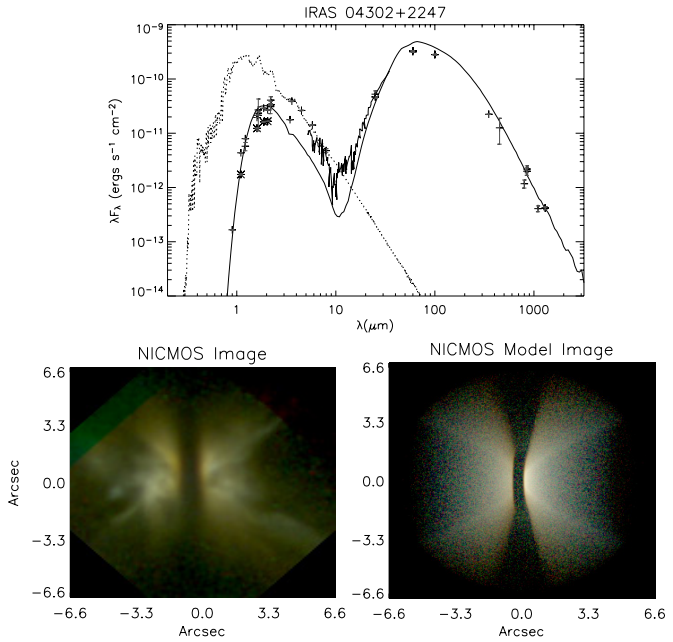

Figure 5. *HST*/NICMOS images model for IRAS 04302+2247 (model b in Table 8, central column). In this case, the SED and the IRS spectrum are ignored. The various panels show the observed and model SEDs, the *HST*/NICMOS image, and the model image similar to Figure 4.

(A color version of this figure is available in the online journal.)

$10^{-8}\,M_{\odot}$ yr^{-1} from high-resolution optical spectra. From our combined model, we obtained a disk mass accretion rate $\dot{M}_{\rm disk} = 1 \times 10^{-8}\,M_{\odot}$ yr^{-1} (see Table 5), in agreement with White & Hillenbrand (2004).

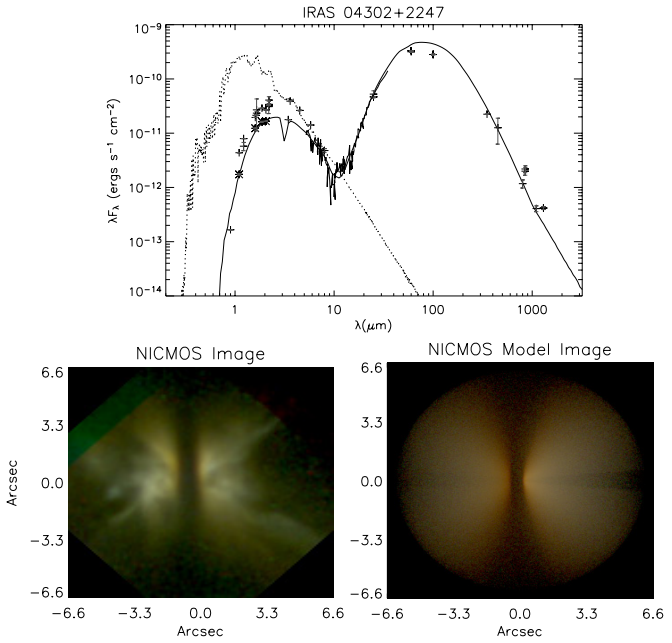

Figure 6. IRAS 04302+2247 combined SED (including the IRS spectrum) and NICMOS images model (model c in Table 8, right column). The various panels show the observed and model SEDs, the *HST*/NICMOS image, and the model image similar to Figure 4.

(A color version of this figure is available in the online journal.)

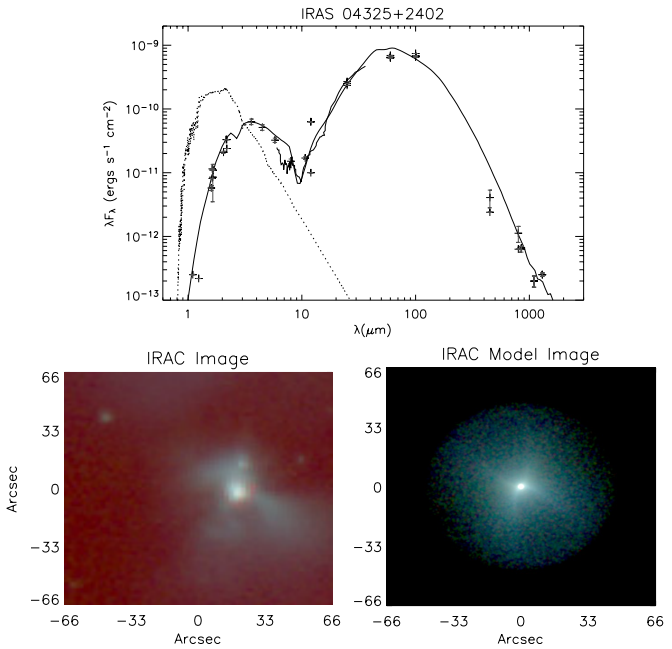

Figure 7. IRAS 04325+2402 combined (SED+images) model (Table 5). The upper panel shows the best combined (SED+images) model SED, the *Spitzer* 5–36 μm spectrum, and the observed fluxes. The dotted line shows the Kurucz model for the stellar photosphere. The bottom left panel shows the *Spitzer*/IRAC image (Padgett et al. 2005), where north is up and east is to the left. The bottom right panel corresponds to the best combined (SED+image) model image.

(A color version of this figure is available in the online journal.)

Eisner et al. (2005) analyzed 1.3 mm (Owens Valley Radio Observatory) and 0.9 μm (Keck) images as well as the SED in the range 8–13 μm, applying a Monte Carlo radiative transfer code (Wolf & Henning 2000; Wolf et al. 2003). They tried four different models corresponding to (1) a rotating infalling

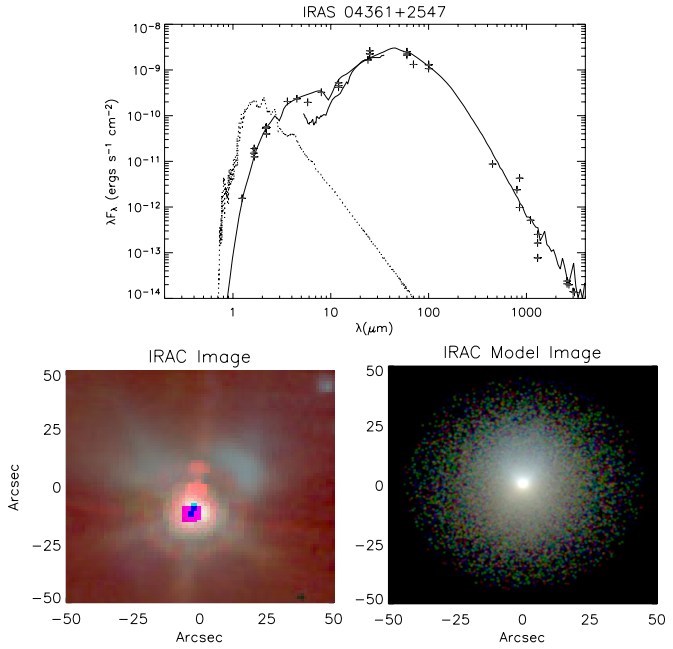

Figure 8. IRAS 04361+2547 combined SED (without the IRS spectrum)+IRAC images model (model a in Table 5). The upper panel shows the SED model, the *Spitzer* 5–36 μm spectrum and the observed fluxes. The dotted line shows the Kurucz model for the stellar photosphere. The bottom left panel shows the *Spitzer*/IRAC image (Padgett et al. 2005), where north is up and east is to the left. The bottom right panel corresponds to the best combined (SED+image) model image.

(A color version of this figure is available in the online journal.)

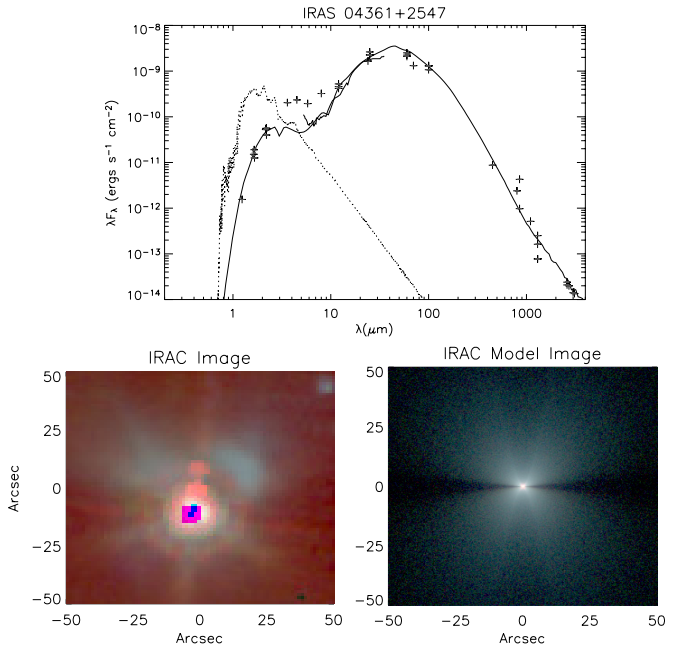

Figure 9. IRAS 04361+2547 combined model including the *Spitzer* spectrum, all compiled fluxes from the literature (see Table 2) but the IRAC fluxes, and the images (model b in Table 5). The upper panel shows the SED model, the *Spitzer* 5–36 μm spectrum, and the observed fluxes. The dotted line shows the Kurucz model for the stellar photosphere. The bottom left panel shows the *Spitzer*/IRAC image (Padgett et al. 2005), where north is up and east is to the left. The bottom right panel corresponds to the model image.

(A color version of this figure is available in the online journal.)

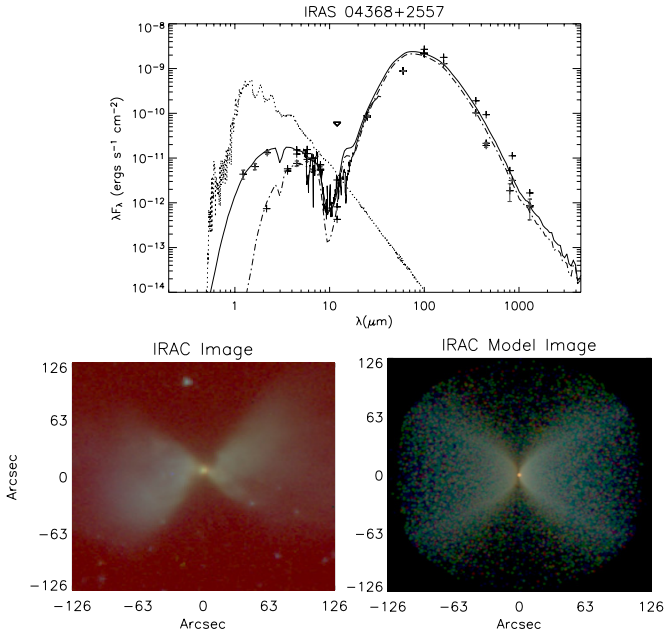

Figure 10. IRAS 04368+2557 combined (SED+images) model (Table 5). The upper panel shows the best combined model SED, the *Spitzer* 5–36 μm spectrum, and the observed fluxes. The upside down triangle corresponds to an upper limit (see Table 2). The dotted line shows the Kurucz model for the stellar photosphere. In this case, we plot the model SED corresponding to two aperture sizes: 26″ (continuous line) and 8″ (dash-dotted) line. The bottom left panel shows the *Spitzer*/IRAC image (Padgett et al. 2005), where north is up and east is to the left. The bottom right panel corresponds to the combined (SED+image) model image.

(A color version of this figure is available in the online journal.)

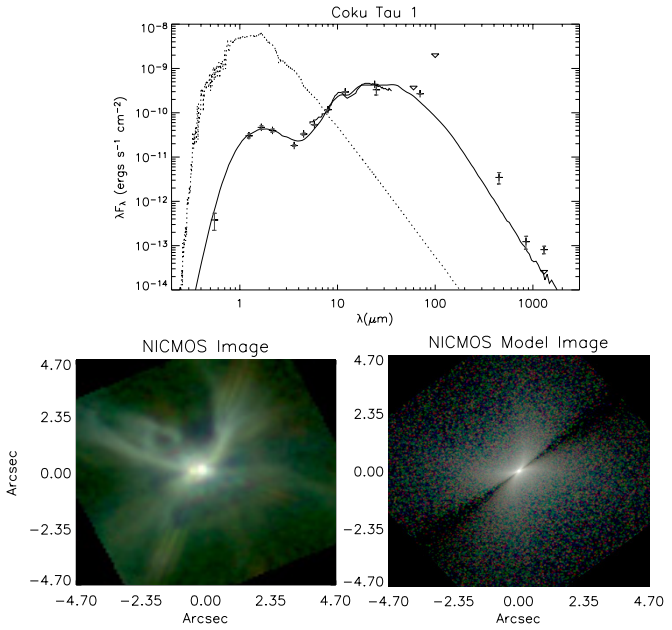

Figure 11. CoKu Tau 1 combined (SED+images) model (Table 5). The upper panel displays the SED model, the *Spitzer* 5–36 μm spectrum, and the observed fluxes, where the upside down triangles correspond to upper limits (see Table 2). The dotted line indicates the Kurucz model for the stellar photosphere. The bottom left panel shows the *HST*/NICMOS image (Padgett et al. 1999), where north is up and east is to the left. The bottom right panel corresponds to the best combined (SED+images) model image.

(A color version of this figure is available in the online journal.)

envelope model, (2) a flared disk model, (3) a disk+envelope model, and (4) a disk+extinction model. We chose to compare our results with those corresponding to model 3, since this model includes both the disk and the envelope. Model parameters

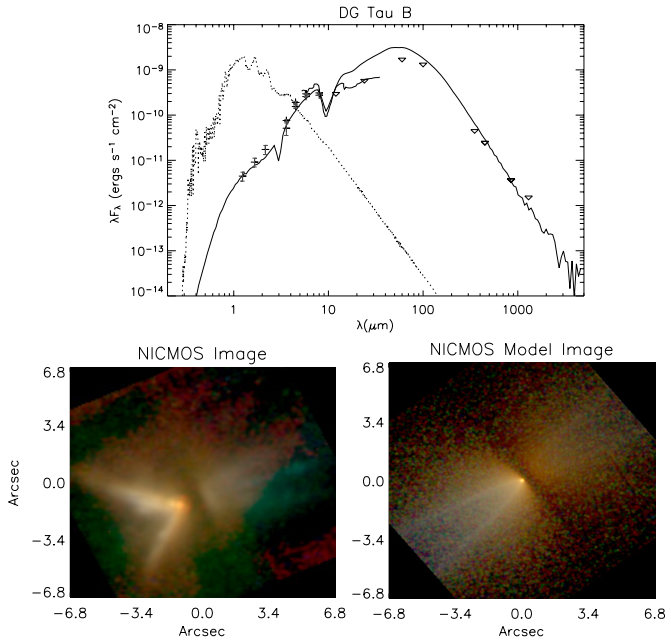

Figure 12. DG Tau B combined (SED+ NICMOS images) model (model a in Table 5). The upper panel displays the SED model, the *Spitzer* 5–36 μm spectrum, and the observed fluxes, where the upside down triangles correspond to upper limits (see Table 2). This model fails to reproduce the SED between 12 and 36 μm. The dotted line indicates the Kurucz model for the stellar photosphere. The bottom left panel shows the *HST*/NICMOS image (Padgett et al. 1999), where north is up and east is to the left. The bottom right panel corresponds to the model image.

(A color version of this figure is available in the online journal.)

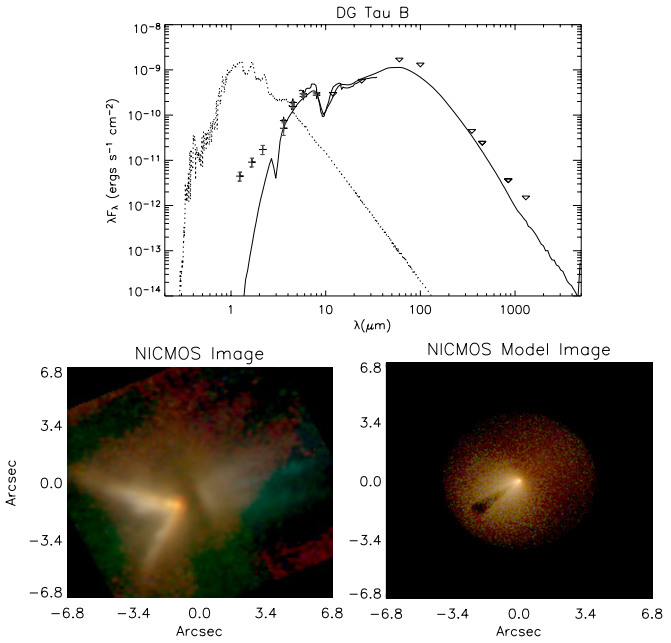

Figure 13. DG Tau B SED without the NICMOS images model (model b in Table 5). The upper panel displays the SED model, the *Spitzer* 5–36 μm spectrum, and the observed fluxes, where the upside down triangles correspond to upper limits (see Table 2). The dotted line indicates the Kurucz model for the stellar photosphere. This model fails to reproduces near-infrared fluxes for wavelengths shorter than 3 μm. The bottom left panel shows the *HST*/NICMOS image (Padgett et al. 1999), where north is up and east is to the left. The bottom right panel corresponds to the model image.

(A color version of this figure is available in the online journal.)

corresponding to Eisner et al.'s (2005) model c are listed in Table 6.

Brinch et al. (2007a) combined published data in 24 molecular transitions (12 species) with observations at 850 μm to describe the structure and dynamics (velocity field) of the envelope of IRAS 04016+2610. Brinch et al. (2007b) focused on the protoplanetary disk of this source, observing the HCO^+ $J = 3$–2 line. From the second work they suggested that the disk is not aligned with the envelope. Table 6 summarizes the parameters derived in both papers.

Gramajo et al. (2007) used the two-dimensional scattering code of Whitney & Hartmann (1993), with the modifications introduced by Whitney & Wolff (2002), to model K and L images of IRAS 04016+2610 (see Table 6). Furlan et al. (2008) modeled the SED (including the *Spitzer* spectrum) of this source using two different models for the collapsing core, a TSC spherically symmetric cloud (Kenyon et al. 1993a) and a sheet-collapse model (Hartmann et al. 1994, 1996). Table 6 lists parameters for their best sheet-collapse model. This model corresponds to $\rho_1 = 4.5 \times 10^{-14}$ g cm^{-3}, which is the density the envelope would have at a radius of 1 AU for the limit $R_c = 0$, proportional to the envelope mass accretion rate and inversely proportional to the square root of the mass of central star. However, they also noticed that with $\rho_1 = 3.5 \times 10^{-14}$ g cm^{-3}, they were able to obtained good fit of the SED with $i = 30°$–$50°$ and $R_c = 70$ AU.

In our combined analysis, we derived an inclination angle, roughly, in agreement with previous determinations (50° versus ~41°, see Table 6). Our final model fits well the absorption feature at 10 μm. The stellar mass, interpolated in the tracks of Siess et al. (2000) and corresponding to the T_{star} measured by White & Hillenbrand (2004) and to the luminosity that scales the SED, ($M_{star} \sim 2.5\ M_\odot$) is larger than derived by Brinch et al. (2007a). A smaller stellar mass would not allow us to reproduce a similar central source as seen in the NICMOS images. Our $M_{disk} = 0.01\ M_\odot$ agrees with Eisner et al. (2005) and Stark et al. (2006), but differs from Brinch et al.'s (2007b) value ($M_{disk} = 0.004\ M_\odot$). However, Brinch et al.'s (2007b) model is quite different from W03b's model. In particular, Brinch et al. (2007b) adopted a flat disk with an angular momentum axis misaligned with respect to the axis of the envelope. In our case, a model SED corresponding to a $0.004\ M_\odot$ M_{disk} does not fit the 10 μm region. Our centrifugal radius, R_c (120 AU), differs from the values determined by Kenyon et al. (1993b, 40 AU) and Whitney et al. (1997, 50 AU) but agrees with other authors (see Table 6). Our M_{env} agrees better with Eisner et al.'s (2005) determination than with Brinch et al.'s (2007b) estimate. For the remaining parameters we find a reasonable good agreement with previous published values.

As already mentioned this source has been previously classified as a transitional Class I–II object (Hogerheijde & Sandell 2000; Park & Kenyon 2002). However, most of the previous works (see, for example, Lada & Wilking 1984; Myers et al. 1987; Kenyon & Hartmann 1995; Hogerheijde et al. 1998) associated this object with a Class I source. From our modeling we derived parameters typical of a Class I object (i.e., $\dot{M}$, R_c, $\dot{M}_{disk}$, M_{disk}, θ, see, for example, W03b).

4.2. IRAS 04248+2612

Also known as HH31 IRS, this is the lowest-mass Class I protostar in Taurus ($M_{star} \sim 0.07\ M_\odot$; White & Hillenbrand 2004). This object is associated with a bipolar outflow (Moriarty-Schieven et al. 1992; Gómez et al. 1997) and is a triple system. Components *A* and *B* have comparable brightness and are

Table 6
Different Models for IRAS 04016+2610

Parameter	Grid Model	Combined Model	Kenyon et al. (1993b)	Whitney et al. (1997)	Eisner et al. (2005)	Stark et al. (2006)	Brinch et al. (2007a)	Brinch et al. (2007b)	Gramajo et al. (2007)	Furlan et al. (2008)
$M_{\rm star}$ ($M_\odot$)	0.44	2.50		0.5	0.50	0.50	∼1.35	1.35		
$R_{\rm star}$ ($R_\odot$)	5.84	2.10		2.00	2.00	2.50				2.00
$T_{\rm star}$ (K)	3615	4580			4000	3800				
$\dot{M}$ ($M_\odot$ yr^{-1})	4.8×10^{-6}	5.0×10^{-6}	4.5×10^{-6}	5.0×10^{-6}	6.0×10^{-6}	1.0×10^{-5}	4.3×10^{-6}		5.0×10^{-6}	
R_c (AU)	47.8	120.0	40.0	50.0	100.0	300.0		200.0	100.0–300.0	100.0
$R_{\rm min}$ ($R_{\rm star}$)	1.0	10.0				3.0				1.0
$R_{\rm max}$ (AU)	2530	5000			2000	5000	2000			6000
$M_{\rm env}$ ($M_\odot$)	0.07	0.06			0.05		0.09			
$M_{\rm disk}$ ($M_\odot$)	0.004	0.010			0.01	0.01		0.004		
$\dot{M}_{\rm disk}$ ($M_\odot$ yr^{-1})	1.2×10^{-7}	1.0×10^{-8}								
A	2.082	2.300				2.250				
B	1.082	1.300				1.250				
θ(°)	3.1	20.0	31.0	26.0		25.0			5.0–10.0	5.0
i(°)	63.2	50.0	60.0	46.0–66.0	37.0	65.0	74.0	40.0	45.0–50.0	40.0
ρ_1 (g cm^{-3})	3.8×10^{-14}	1.7×10^{-14}								4.5×10^{-14}
$L_{\rm tot}$ ($L_\odot$)	5.47	4.51				3.70				4.50

Note. Symbols for model parameters are as indicated in Table 3.

Table 7
Different Models for IRAS 04248+2612

Parameter	Grid Model	Combined Model	Kenyon et al. (1993a)	Lucas & Roche (1997)	Whitney et al. (1997)	Stark et al. (2006)	Furlan et al. (2008)
$M_{\rm star}$ ($M_\odot$)	0.22	0.07			0.50	0.50	
$R_{\rm star}$ ($R_\odot$)	2.33	0.90			2.00	2.50	2.00
$T_{\rm star}$ (K)	3131	2845				3800	
$\dot{M}$ ($M_\odot$ yr^{-1})	1.1×10^{-5}	4.4×10^{-6}			1.0×10^{-6}	1.0×10^{-6}	
R_c (AU)	109	60	70		100	50	30
$R_{\rm min}$ ($R_{\rm star}$)	54.2	11.7				5373.6	5.0
$R_{\rm max}$ (AU)	2122	9000				5000	10000
$M_{\rm env}$ ($M_\odot$)	0.15	0.10					
$M_{\rm disk}$ ($M_\odot$)	0.005	0.010				0.01	
$\dot{M}_{\rm disk}$ ($M_\odot$ yr^{-1})	1.4×10^{-7}	1.0×10^{-8}					
A	2.135	2.280				2.250	
B	1.135	1.280				1.250	
θ(°)	14.5	16.0		15.0	26.0	20.0	15.0
i(°)	69.5	65.0	30.0	78.0	78.0–90.0	76.0	70.0
ρ_1(g cm^{-3})	1.2×10^{-13}	8.8×10^{-14}	3.2×10^{-14}				4.0×10^{-15}
$L_{\rm tot}$ ($L_\odot$)	0.47	1.05	0.36			0.37	0.40

Note. Symbols for model parameters are as indicated in Table 3.

separated by 0.″16 (Padgett et al. 1999); the third component (C) is located 4.″55 of the AB pair (Duchene et al. 2004). In our analysis we treat the close binary as a single source. Since it is illuminating a much larger envelope and a disk with a large inner hole, this should not affect the derived envelope/disk parameters.

The SED constructed from fluxes published in the literature does not cover very well the silicate feature at 10 μm. Fortunately the *Spitzer*/IRS 5–36 μm spectrum obtained by Furlan et al. (2008) includes this region and shows small emission around 10 μm. Far-infrared and submillimeter fluxes are scarce and the SED is not well defined in this spectral region. Images obtained with both the *HST*/NICMOS and the *Spitzer*/IRAC are available for this source. The NICMOS images show a long curved bipolar reflection nebula, while IRAC images display an elongated nonsymmetrical structure.

Similar to our analysis of IRAS 04016+2610, in our analysis of IRAS 04248+2612, we fixed the stellar temperature ($T_{\rm star}$ = 2845 K) to the value derived by White & Hillenbrand (2004) and carried out the combined SED and image modeling. Table 4 lists the best-fit model derived from the grid of R06, and Table 5 and Figure 3 show the best combined model.

Our best model images resemble the *HST* and *Spitzer* images. This model also fits the mid-infrared spectrum and reproduces the observed fluxes with exception of the millimeter region, where the model underestimates the fluxes (see also Furlan et al. 2008). To be able to fit the millimeter region of the SED we need to increase R_c, θ, and $\dot{M}$, which does not provide a good fit to the infrared region of the SED and, in addition, produces model images that do not resemble the shape of the NICMOS+IRAC images. The observed fluxes in the millimeter region could be associated with dust outside the infall zone that do not belong to the star+disk+envelope system, but rather corresponds to the surrounding cloud (Jayawardhana et al. 2001; Furlan et al. 2008). Alternatively, it could be due to external heating of the cloud by the interstellar radiation field. Our recent models that include this effect show an increase in long-wavelength radiation (B. A. Whitney et al. 2010, in preparation). Table 7 compares the best-fit R06 grid model (see Table 4), our combined model (see Table 5) and different models

from the literature for IRAS 04248+2612. The inclusion of the NICMOS images in our modeling provides better constrains to the inclination angle (i: 65.°0 versus 69.°5), and to the cavity opening angle (θ: 16.°0 versus 14.°5). The modeling of the IRAC images introduces modifications in several parameters, such as the mass of the disk ($M_{\rm disk}$: 0.010 $M_\odot$ versus 0.005 $M_\odot$), the disk mass accretion rate ($\dot{M}_{\rm disk}$: 1.0×10^{-8} $M_\odot$ yr^{-1} versus 1.4×10^{-7} $M_\odot$ yr^{-1}), the disk radial density exponent (A: 2.280 versus 2.135), the disk scale height exponent (B: 1.280 versus 1.135), the centrifugal radius (R_c: 60 AU versus 109 AU), and the inner radius of the disk ($R_{\rm min}$: 11.7 $R_{\rm star}$ versus 54.2 $R_{\rm star}$).

Padgett et al. (1999) estimated an opening angle $\theta = 30.°0$. We derived an opening angle $\theta = 16.°0$, in reasonable agreement for a curved cavity, since ours is measured at the outer radius of the envelope, which is here 9000 AU. Andrews & Williams (2005) and Ohashi et al. (1996) derived $M_{\rm disk} = 0.005$ $M_\odot$ and $M_{\rm disk} < 0.034$ $M_\odot$, respectively. We obtained $M_{\rm disk} = 0.01$ $M_\odot$, within the range of previous estimate. From the *HST*/NICMOS images Stark et al. (2006) suggested that the inclination of this source is close to edge-on. We derived a lower inclination angle ($i = 65.0$) from our combined model. White & Hillenbrand (2004) derived a disk mass accretion rate for this source 1 order of magnitude lower than our combined model ($\dot{M}_{\rm acc} = 1.0 \times 10^{-9}$ $M_\odot$ yr^{-1} versus $\dot{M}_{\rm disk} = 1.0 \times 10^{-8}$ $M_\odot$ yr^{-1}).

Kenyon et al. (1993a) modeled the SED of IRAS 04248+2612 using a 1.5-dimensional radiative transfer code. Lucas & Roche (1997) analyzed low-resolution near-infrared images of this object using a scattering model. Whitney et al. (1997) analyzed the low-resolution near-infrared images. Stark et al. (2006) modeled the *HST*/NICMOS images of IRAS 04248+2612. Furlan et al.'s (2008) model fits better the short-wavelength part of the SED than the far-infrared and millimeter region. Table 7 summarizes parameters derived from previous modeling attempts.

Table 7 shows a good agreement between our combined (SED+images) model and those from the literature, in particular with respect to $M_{\rm disk}$ and $\dot{M}$. For $R_{\rm c}$ we obtained a value of 60 AU, roughly in between the values determined by Whitney et al. (1997, $R_{\rm c} = 100$ AU) and Furlan et al. (2008, $R_{\rm c} = 30$ AU), and in agreement with the other authors. We note that $R_{\rm c} < 60$ AU produces less extended images that do not resemble those shown in Figure 3 (left panels). Our inclination angle ($i = 65.°0$) agrees with other determinations but differs with Kenyon et al.'s (1993a) estimate ($i = 30.°0$). In addition our $R_{\rm min}$ ($= 11.7 R_{\rm star}$) is quite different from $R_{\rm min} = 5373.6 R_{\rm star}$ derived by Stark et al. (2006). For the stellar parameters, we obtained $R_{\rm star} = 0.9$ $R_\odot$ and $M_{\rm star} = 0.07$ $M_\odot$. This is an over-estimate of the most massive star in the binary pair since it assumes a single source. The central source mass currently lies within the brown dwarf regime. However, it may continue to grow until the main accretion phase ends.

4.3. IRAS 04302+2247

This Class I source lies almost edge-on in the plane of the sky and displays a scattered-light bipolar nebula with approximately the same brightness in the Eastern and Western lobes. Bontemps et al. (1996) detected a bipolar molecular outflow associated with IRAS 04302+2247. For this object we modeled the SED, including the *Spitzer* spectrum, and the NICMOS images.

The SED shows a deep, absorption feature at 10 μm. The *Spitzer* spectrum delineates this feature. W03a showed that such an absorption feature at 10 μm can result from an edge-on disk extincting all of the direct stellar flux and mid-IR flux from the inner warm disk. The SED consists therefore of two components: a scattered stellar/inner disk spectrum peaking at 2 μm, and the thermal radiation from the less obscured and therefore cooler dust in the disk and envelope. NICMOS images show a nebula crossed by an opaque band extending 900 AU north–south. No central point object is apparent in these images.

Table 8
IRAS 04302+2247: Different Model Attempts

Parameter	Model a[a]	Model b[b]	Model c[c]
$\dot{M}$ ($M_\odot$ yr^{-1})	1×10^{-6}	1.7×10^{-6}	9×10^{-6}
R_c (AU)	250	500	500
$R_{\rm min}$ ($R_{\rm star}$)	60	40	20
$R_{\rm max}$ (AU)	1870	1870	1870
$M_{\rm disk}$ ($M_\odot$)	0.07	0.30	0.07
$\dot{M}_{\rm disk}$ ($M_\odot$ yr^{-1})	4.4×10^{-9}	1×10^{-9}	5.4×10^{-10}
A	2.14	2.18	2.22
B	1.14	1.18	1.22
θ(°)	33	33	6
i(°)	80	83	83
$\rho_{\rm cav}$ (g cm^{-3})	2.6×10^{-21}	2.6×10^{-21}	1.5×10^{-16}

Notes.
[a] Model of the SED, including IRS spectrum but ignoring NICMOS fluxes (see Figure 4).
[b] NICMOS images model (see Figure 5). In this case, we disregarded the SED and the IRS spectrum.
[c] Combined model for the SED(+IRS spectrum) and the NICMOS images (see Figure 6).

Table 4 lists the best-fit SED model derived from the grid of R06. As a first attempt to fit the source, we modeled the SED, including the IRS spectrum, but ignore the fluxes from the NICMOS images (model a, Table 8 left column and Figure 4). This model does not reproduce the *HST* images. The central band (the disk) in the model image is not as nearly as broad as in the observed NICMOS data. The parameters corresponding to this model are, in general, different from those obtained from the grid analysis. To obtain a better match to the NICMOS images, we need a more edge-on disk as well as larger A (disk radial density) and B (disk scale height) exponents (i.e., thicker disks with a larger flare). Figure 5 and Table 8, central column (model b), show a model that gives a better match to the NICMOS images but that produces a very poor approximation to the SED and the IRS spectrum. The parameters corresponding to the disk in this model significantly differ from those obtained in the previous attempt. We then searched for a combined model that produces a compromise between an acceptable SED, including the IRS spectrum, and image fits.

We initially considered the difference between the parameter values in the left and central columns of Table 8 and their influences on the images and the SED, respectively. For example, increasing the inclination angle from 80° to 83°, we obtained a model SED with a deeper absorption feature around 10 μm than that shown by the *Spitzer* spectrum. In the same manner, larger A and B values give an SED that underestimates observed fluxes in the near- and mid-infrared spectral regions. Conversely, if we adopt the inclination angle corresponding to a good SED model (model a), the resultant images do not resemble *HST* images. The *HST* images clearly show that we need an edge-on large disk, and the resultant SED fit shows that we need more near-IR scattered light. Thus, we chose to increase the density in the outflow cavity to provide more scattered light. This parameter also affects the shape of the SED between 10 and 100 μm and thus we also needed to modify other parameters, such as $\dot{M}_{\rm disk}$, $R_{\rm min}$,

Table 9
Different Models for IRAS 04302+2247

Parameter	Grid Model	Combined Model	Kenyon et al. (1993a)	Lucas & Roche (1997)	Whitney et al. (1997)	Stark et al. (2006)	Furlan et al. (2008)
$M_{\rm star}$ ($M_\odot$)	0.19	0.50			0.50	0.50	
$R_{\rm star}$ ($R_\odot$)	2.85	2.85			2.00	2.50	2.00
$T_{\rm star}$ (K)	3024	3800				3800	
$\dot{M}$ ($M_\odot$ yr^{-1})	2.8×10^{-5}	9.0×10^{-6}			2.0×10^{-6}	2.5×10^{-6}	
R_c (AU)	57.9	500.0	70.0		10.0	300.0	300.0
$R_{\rm min}$ ($R_{\rm star}$)	98.6	20.0				3.0	1.0
$R_{\rm max}$ (AU)	5786	1870				5000	10000
$M_{\rm env}$ ($M_\odot$)	0.31	0.12					
$M_{\rm disk}$ ($M_\odot$)	0.001	0.070				0.070	
$\dot{M}_{\rm disk}$ ($M_\odot$ yr^{-1})	4.4×10^{-9}	5.4×10^{-10}					
A	2.136	2.220				2.250	
B	1.136	1.220				1.250	
θ(°)	32.5	6.0		75.0	26.0	25.0	22.0
i(°)	31.8	83.0	60.0	90.0	78.0-90.0	85.0	89.0
ρ_1(g cm^{-3})	3.4×10^{-13}	6.8×10^{-14}	1.0×10^{-13}				3.0×10^{-14}
$L_{\rm tot}$ ($L_\odot$)	0.62	1.52	0.33			0.44	1.00

Note. Symbols for model parameters are as indicated in Table 3.

$M_{\rm disk}$, R_c, $\dot{M}$, and A and B. In particular, A and B are relevant as they are larger than in "typical" Class I objects (W03a).

Our best combined model (model c), shown in Table 8 (right column) and Figure 6, fits very closely the mid-infrared spectrum and the near-infrared fluxes from Padgett et al. (1999), the asterisks in Figures 4, 5, and 6. The other near-IR data were taken in a larger beam and are therefore expected to have higher fluxes (Whitney et al. 1997). In general, the combined model as well as our model b that matches the *HST* images reproduces well the central dark lane seen in the *HST* images.

In Table 9, we list the R06 grid model (see Table 4), our combined model (see Table 5 or model c in Table 8, right column) and different models from the literature. The inclusion of the NICMOS images in our models helped us to better determine the inclination angle (i: 83.°0 versus 31.°8).

Padgett et al. (1999) derived a cavity opening angle $\theta = 30.°0$ based on the *HST*/NICMOS images. Andrews & Williams (2005) estimated $M_{\rm disk} = 0.03\,M_\odot$ from submillimeter data while Wolf et al. (2008) obtained $M_{\rm disk} = 0.07\,M_\odot$ from 850 μm data. Our combined model gives a cavity opening angle ($\theta = 6.°0$), rather small in comparison with Padgett et al.'s (1999). However models a and b, as well as the R06 grid model, provide a cavity opening angle in agreement with Padgett et al. (1999). Our estimate for the disk mass ($M_{\rm disk} = 0.07\,M_\odot$) agree with previous determinations.

Several groups have modeled this source. Lucas & Roche (1997) noted that the shape of the nebula resembles the wings of a butterfly, and thus called it "*the butterfly star*". They interpreted the quadrupolar morphology of IRAS 04302+2247 as an edge-on infalling envelope and a bipolar outflow perpendicular to the dark lane. Whitney et al. (1997) modeled low-resolution near-infrared images, using a two-dimensional Monte Carlo radiative transfer code based on the TSC cloud core. Stark et al. (2006) modeled the *HST* images and Furlan et al. (2008) the SED.

For IRAS 04302+2247 we derived a large $M_{\rm disk}$ (0.07 $M_\odot$, see Table 5) in agreement with Stark et al.'s (2006) estimate (see Table 9). The disk mass accretion rate is among the most poorly determined for the complete sample because the inner disk region and its mid-IR flux are blocked from view. As mentioned before no central object appears in the *HST* images. Our model predicts a low mass central star ($M_{\rm star} = 0.5\,M_\odot$) with a radius of 2.85 $R_\odot$ and a temperature of 3800 K.

In general our results agree with previous works (see Table 9). In particular, we find a good agreement for A, B, and $M_{\rm disk}$. However, our cavity opening angle ($\theta = 6.°0$) is smaller than other determinations ($\theta = 22.°0$–$75.°0$). In addition our centrifugal radius, $R_{\rm c}$, agrees with Stark et al. (2006) and Furlan et al. (2008), but differs from the values determined by Kenyon et al. (1993a) and Whitney et al. (1997). However, Whitney et al.'s (1997) result ($R_{\rm c} = 10$ AU) was based on low-resolution near-infrared images and did not resolve the large disk. With $R_{\rm c} < 200$ AU, the model SED does not fit the fluxes in the near-infrared and in the submillimeter regions. In addition, the model images appear less extended than the observed images.

4.4. IRAS 04325+2402

Also known as L1535 IRS, this source exhibits a complex bipolar scattered light nebula, associated with a molecular outflow (Moriarty-Schieven et al. 1992; Hogerheijde et al. 1998). *HST*/NICMOS observations resolved this object into a central binary (A/B) source and its companion (C), seen nearly edge-on through a dusty disk and envelope (Hartmann et al. 1999). These authors also suggested that the system may have multiple centers of infall and non-aligned outflows and disks.

The SED and the *Spitzer* 5–36 μm spectrum show a dip around 10 μm, similar to IRAS 04302+2247, and suggest an edge-on source (W03a). The SED also shows a secondary peak around 100 μm. The IRAS 04325+2405 IRAC image displays a bipolar reflection nebula with a southwest lobe more extended than the other, and with a U-shape. In this image, we can distinguish the three components mentioned before although we consider this object as a single star in our analysis. Our model, derived applying the grid of the R06, is listed in Table 4. The combined (SED+images) model is shown in Table 5 and Figure 7.

We obtained a good fit to the SED in the near-infrared. In Table 2 at 12 μm, we list two values: an upper limit (from the IRAS point source catalog) and a measurement from Clark (1991). Our best model falls between these two fluxes. However, since the IRS spectrum is available in this case, the sometimes uncertain IRAS fluxes are less relevant. In addition our model lies close to the IRS spectrum.

Table 10
Different Models for IRAS 04325+2402

Parameter	Grid Model	Combined Model	Kenyon et al. (1993a)	Whitney et al. (1997)	Furlan et al. (2008)
M_{star} ($M_\odot$)	0.41	0.41		0.50	
R_{star} ($R_\odot$)	3.17	3.17		2.00	2.00
T_{star} (K)	3617	3150			
$\dot{M}$ ($M_\odot$ yr^{-1})	2.9×10^{-6}	2.9×10^{-6}		5.0×10^{-6}	
R_c (AU)	68.9	68.9	300.0	50.0	~100.0
R_{min} (R_{star})	159.4	661.1			3.0
R_{max} (AU)	4190	3500			5000
M_{env} ($M_\odot$)	0.72	0.12			
M_{disk} ($M_\odot$)	0.001	0.0001			
$\dot{M}_{disk}$ ($M_\odot$ yr^{-1})	6.2×10^{-10}	6.2×10^{-10}			
A	2.178	2.180			
B	1.178	1.180			
θ(°)	32.9	20.0		11.0	15.0
i(°)	69.5	55.0	60.0	72.0–90.0	80.0
ρ_1(g cm^{-3})	2.4×10^{-14}	2.4×10^{-14}	1.0×10^{-13}		3.0×10^{-14}
L_{tot} ($L_\odot$)	1.54	1.21	0.72		0.90

Note. Symbols for model parameters are as indicated in Table 3.

Our model does not reproduce the shape of the SED between 5 and 36 μm perfectly. Furlan et al. (2008) noted that the spectrum has a peculiar shape in this region maybe due to the binarity of the central source. Finally, observed submillimeter fluxes have a large dispersion and our best model does not appear at first look to reproduce the flux at 450 μm. However, the observed flux corresponds to a relatively small aperture (~9″; see Table 2). The model SED corresponding to an aperture of 9″ does fit this point.

Table 10 summarizes different models for IRAS 04325+2402, including the R06 grid model (see Table 4), our combined model (see Table 5) and previously published model (Kenyon et al. 1993a; Whitney et al. 1997; Furlan et al. 2008).

The inclusion of the IRAC images in the modeling of IRAS 04325+2402 produces different values in comparison to the R06 grid for the disk mass (M_{disk}: 0.0001 $M_\odot$ versus 0.001 $M_\odot$), and the disk inner radius (R_{min}: 661.1 R_{star} versus 159.4 R_{star}). In addition, $\dot{M}_{disk}$, A (the disk radial density exponent), and B (the disk scale height exponent) were not changed by the IRAC image modeling.

Hogerheijde et al. (1998) estimated an inclination angle $i = 60°$ from the ^{12}CO 3–2 molecular outflow. Andrews & Williams (2005) and Ohashi et al. (1996) derived $M_{disk} = 0.008\ M_\odot$ and $M_{disk} < 0.021\ M_\odot$, respectively. Our determination for the inclination to the line of sight ($i = 55.0$) is in good agreement with Hogerheijde et al. (1998). However, the mass of the disk derived from our combined model ($M_{disk} = 0.0001\ M_\odot$) is lower than previous estimates.

Our inclination angle agrees with the determinations of Hogerheijde et al. (1998) and Kenyon et al. (1993a), but differs from the value obtained by Furlan et al. (2008). A model SED for $i \sim 80°$, as in Furlan et al.'s (2008) model, does not provide a good fit in the far-infrared region. However our $R_c \sim 70$ AU agrees with the value obtained by Whitney et al. (1997) and Furlan et al. (2008) and differs from the value obtained by Kenyon et al. (1993a). For $R_c > 100$ AU the model SED shows a deeper absorption at 10 μm, and model images appear more extended than what is observed. Our determination for R_{min} (~600 R_{star}) differs from Furlan et al.'s (2008) estimate (~3 R_{star}). Finally, the values derived for θ and $\dot{M}$ roughly agree with those obtained by other authors.

4.5. IRAS 04361+2547

Also known as TMR 1, this source is a Class I object associated with a bipolar outflow (Terebey et al. 1990; Bontemps et al. 1996; Hogerheijde et al. 1998) and surrounded by an opaque infalling envelope (Kenyon et al. 1993a; Terebey et al. 1990). This object is a close binary system. Terebey et al. (2000) found that the companion is separated by ~0.″31.

The dispersion in the near-infrared region of the SED is probably due to the variability of this source (Park & Kenyon 2002). The SED shows a broad contribution in the near- and mid-infrared region with a peak around 100 μm while millimeter data have a large scatter. The *Spitzer* spectrum seems to show a combination of an absorption and an emission component around 10 μm. However *Spitzer* 5–36 μm fluxes do not match fluxes compiled from the literature. The IRAC images of IRAS 04361+2547 show a bright point source with a faint extended bipolar nebulosity in the north–south direction. The Northern lobe is dominated by the [3.6] filter contribution (in blue). As for previous objects we model this object as a single star.

In Table 4, the best-fit SED model derived from the grid of R06 is listed. For the combined analysis, since the broadband SED and *Spitzer* IRS spectra disagree, we present two models: one for the SED, without the IRS spectrum, and the IRAC images (model a, in Table 5 and Figure 8) and another one for the *Spitzer* spectrum, all compiled fluxes but the IRAC fluxes and including the IRAC images (model b, in Table 5 and Figure 9). The discrepancy between the IRS spectrum and the IRAC fluxes is likely due to an aperture effect. The IRS slit width in this wavelength region is only 3.″6, whereas IRAC fluxes were obtained with an aperture of 35″ (Robitaille et al. 2007). Due to the dispersion in the millimeter region of the observed SED we adopted a model SED that reproduces average values of the observed fluxes.

In Table 11, we summarize different models from the literature for IRAS 04361+2547 as well as R06's grid model (see Table 4) and our combined models (see Table 5). In particular, Table 11 lists parameters from the models by Kenyon et al. (1993a), Whitney et al. (1997), Gramajo et al. (2007, derived from *L*-band images), and Furlan et al. (2008). IRAC images

Table 11
Different Models for IRAS 04361+2547

Parameter	Model of R06	Combined Model a[a]	Combined Model b[b]	Kenyon et al. (1993a)	Whitney et al. (1997)	Gramajo et al. (2007)	Furlan et al. (2008)
M_{star} ($M_\odot$)	0.21	0.80	0.35		0.50		
R_{star} ($R_\odot$)	4.89	3.10	3.80		2.00		2.00
T_{star} (K)	3092	4100	4100				
$\dot{M}$ ($M_\odot$ yr^{-1})	5.6×10^{-6}	1.3×10^{-6}	4.2×10^{-6}		5.0×10^{-6}	2-5.0 $\times 10^{-6}$	
R_c (AU)	7.6	40.0	50.0	10.0	50.0	30.0-50.0	100.0
R_{min} (R_{star})	1.0	2.0	50.0				2.0
R_{max} (AU)	2368	3600	3600				10000
M_{env} ($M_\odot$)	0.10	0.02	0.02				
M_{disk} ($M_\odot$)	0.001	0.001	0.001				
$\dot{M}_{disk}$ ($M_\odot$ yr^{-1})	1.1×10^{-7}	1.1×10^{-7}	1.1×10^{-7}				
A	2.037	2.200	2.040				
B	1.037	1.200	1.040				
θ(°)	8.5	8.4	10.0		11.0	15.0	15.0
i(°)	18.2	18.2	70.0	30.0	72.0-90.0	72.0-75.0	80.0
ρ_1(g cm^{-3})	6.5×10^{-14}	7.7×10^{-15}	3.8×10^{-14}	3.2×10^{-14}			2.0×10^{-14}
L_{tot}($L_\odot$)	2.09	2.51	3.67	2.88			4.00

Notes. Symbols for model parameters are as indicated in Table 3.
[a] Model a corresponds to the SED, without the IRS spectrum, and the images (see Figure 8).
[b] Model b fits the *Spitzer* spectrum, all compiled fluxes from the literature (see Table 2) but the IRAC fluxes and the images (see Figure 9).

introduce modifications in some of the parameters of both models a and b, such as the centrifugal radius (R_c: 40 −50 AU versus 7.6 AU) and the disk inner radius (R_{min}: 2.0 R_{star}—model a—50.0 R_{star}—model b—versus 1.0 R_{star}). The inclination to the line of sight was changed only for model b (i: 70° versus 18.°2), while the disk radial density exponent and the disk scale height exponent were modified for model a (A: 2.20 versus ∼2.04, B: 1.2 versus ∼1.04). The mass of disk (M_{disk}) and the mass accretion rate ($\dot{M}_{disk}$) were not changed by the inclusion of IRAC images in our modeling.

From the ^{12}CO 3–2 molecular outflow Hogerheijde et al. (1998) estimated $i = 60°$. Andrews & Williams (2005) and Ohashi et al. (1996) derived $M_{disk} = 0.01\,M_\odot$ and $M_{disk} = 0.032\,M_\odot$, respectively. For the inclination angle we derived two different values corresponding to model a ($i = 18.2$) and model b ($i = 70.0$). The later model agrees better with Hogerheijde et al.'s (1998) estimate. In the case of the mass of the disk, both models a and b give a value ($M_{disk} = 0.001\,M_\odot$) an order of magnitude lower than submillimeter/millimeter estimates. The submillimeter/millimeter estimates are likely more accurate.

Both our models show a weak absorption at 10 μm. However, the stellar parameters corresponding to models a and b differ. For L_{tot} we obtained 2.51 $L_\odot$ and 3.67 $L_\odot$, for the SED+images and IRS spectrum models, respectively. In the case of M_{star}, we derived 0.80 and 0.35 $M_\odot$, respectively.

While the differences in $\dot{M}_{disk}$, R_c, and θ are not significant for these models, the inclination angle differs by ∼50° between both models. The inclination angle corresponding to the SED, without the IRS spectrum, and the IRAC images model (model a) is smaller than in previous works (18.°2 versus 30–90°). The model that fits the *Spitzer* spectrum (model b) has a larger inclination (70°) in better agreement with previous results. In addition, this second model reproduces the bipolar nebulosity surrounding the central star. Overall, our preferred fit is model b. IRAC fluxes for this object should be used with caution.

Our results suggest the presence of a small disk ($M_{disk} \sim 0.001\,M_\odot$) with a significant mass accretion rate ($\dot{M}_{disk} = 1.1 \times 10^{-7}\,M_\odot$ yr^{-1}). The envelope accretion rate ($\dot{M}$) and the cavity opening angle (θ) agree with previous determinations. Our centrifugal radius, R_c, for models a and b (40 and 50 AU, respectively) agrees with other models with exception of Furlan et al.'s estimate ($R_c = 100$ AU).

4.6. IRAS 04368+2557

Also known as L1527, a Class 0/I object (André et al. 2000; Motte & André 2001), associated with a bipolar outflow (Bontemps et al. 1996; Hogerheijde et al. 1998), this IRAS source is a binary system with a separation of ∼0.″17 (Loinard et al. 2002). A third faint companion is located at a distance of 20″ (Fuller et al. 1996; Hogerheijde et al. 1998).

The SED and the *Spitzer* spectrum have a deep dip at 10 μm, as in IRAS 04302+2247, again, likely due to obscuration of the star/inner disk due to its edge-on orientation (W03a). The SED shows a peak around 100 μm (see Figure 10). The flux around 10 μm is only an upper limit and was not taken into account in our modeling (see Table 2). The near- and mid-infrared fluxes taken from the literature were measured using different apertures. The IRAC images for IRAS 04368+2557 show a central source associated with an elongated bipolar reflection nebula. As for other sources we analyze this object as a single target and present in Table 4 the best SED result derived from the R06 models. In Table 5 and Figure 10, we show our combined (SED+images) model.

Some of the near-IR data were taken in two different apertures (26″ and 8″). In Figure 10, we plot the same model corresponding to these two apertures. Our best model reproduces well the SED and the spectrum in both apertures. However, this SED model overestimates the observed flux at 60 μm (see Table 2). We made several tests to try to fit this point. For example with $\theta = 24°$, we found a model that produces a good match from 60 μm to the millimeter region but does not reproduce the observed fluxes in the near- and mid-infrared part of the SED. Conversely with $\dot{M} = 6 \times 10^{-6}\,M_\odot$ yr^{-1}, we are able to fit the near- and mid-infrared region as well as the flux at 60 μm but this model underestimates the contribution of the *Spitzer* spectrum and millimeter fluxes.

Our model image shows a tenuous central source surrounding by a relatively thin dark lane (the disk) in comparison to the observed IRAC images (see Figure 10). Recently, Tobin et al. (2008) noticed the same peculiarity in their model image of

Table 12
Different Models for IRAS 04368+2557

Parameter	Grid Model	Combined Model	Kenyon et al. (1993a)	Tobin et al. (2008)	Furlan et al. (2008)
M_{star} ($M_\odot$)	0.13	0.70		0.50	
R_{star} ($R_\odot$)	4.05	3.00		2.09	2.00
T_{star} (K)	2741	4000		4000	
$\dot{M}$ ($M_\odot$ yr^{-1})	3.7×10^{-5}	3.0×10^{-5}		1.0×10^{-5}	
R_c (AU)	9.5	250.0	300.0	75.0	200.0
R_{min} (R_{star})	136.2	7.0		14.25	1.0
R_{max} (AU)	2977	5000		15000	10000
M_{env} ($M_\odot$)	1.26	0.82			
M_{disk} ($M_\odot$)	0.001	0.060		0.1	
$\dot{M}_{disk}$ ($M_\odot$ yr^{-1})	4.5×10^{-8}	3.0×10^{-7}		3.0×10^{-7}	
A	2.250	2.300		2.125	
B	1.220	1.300		1.125	
θ(°)	7.1	30.0			27.0
i(°)	18.2	80.0	60.0-90.0	85.0	89.0
ρ_1(g cm^{-3})	5.4×10^{-13}	1.9×10^{-13}	3.2×10^{-13}	3.8×10^{-14}	4.0×10^{-14}
L_{tot} ($L_\odot$)	0.87	3.98	1.35	2.75	1.80

Note. Symbols for model parameters are as indicated in Table 3.

this source and modified the geometry of the inner envelope introducing a "dual-cavity" (i.e., two outflow cavities: one narrow cavity near the central source and wider cavity offset form the central object). They adopted a curved cavity described by the expression $z = C(x^2+y^2)^{b/2}$, where C is a constant given by a relation between the opening angle of the cavity and the radius of the envelope. The exponent b is related with the shape of the cavity; b_{in} corresponds to the internal cavity and b_{out} to the external cavity. The adopted values are $b_{in} = 1.5$ and $b_{out} = 1.9$. This modification, introduced to the W03a code, allowed the authors to obtain model images with an apparent (bright) point source from light scattered in the inner cavity and a thin central dark lane between the cavities produced by the shadow of the inner cavity on the outer cavity.

In Table 12, we compare R06's grid model (see Table 4), our combined model (see Table 5), and those from the literature (Kenyon et al. 1993a; Tobin et al. 2008; Furlan et al. 2008). The modeling of the IRAC images allowed us to better constrain the inclination to the line of sight (i: 80° versus 18.°2) and the cavity opening angle (θ: 30° versus 7.°1). Other parameters, such as the mass of the disk (M_{disk}: 0.06 $M_\odot$ versus 0.001 $M_\odot$) and the disk mass accretion rate ($\dot{M}_{disk}$: 3×10^{-7} $M_\odot$ yr^{-1} versus 4.5×10^{-8} $M_\odot$ yr^{-1}), were also modified by the inclusion of the IRAC images in our modeling attempt.

Hogerheijde et al. (1998) estimated $i = 75°$ from the ^{12}CO 3–2 molecular outflow. Andrews & Williams (2005) derived $M_{disk} = 0.04\ M_\odot$ using millimeter data. The values for both the inclination angle ($i = 80.°0$) and the mass of the disk ($M_{disk} = 0.06\ M_\odot$) derived from our model (see Table 5) agree with these determinations.

Tobin et al.'s (2008) model corresponds to the "dual-cavity" model, with opening angles of 15° (θ_{in}) and 20° (θ_{out}). In our combined model attempt, we used a "single-cavity" approximation and derived the parameters listed in Table 5. In general, we find that non-geometry-dependent parameters (such as stellar parameters, $\dot{M}$, $\dot{M}_{disk}$, M_{disk}, i) roughly agree with those derived by Tobin et al. (2008). Not surprisingly, those directly associated with the morphology of the cavity (such as θ, R_{max}, R_{min}, R_c) are different. In particular, our model has a single cavity with $\theta = 30°$ and $b = 1.5$. In addition we note that Furlan et al. (2008) obtained a total luminosity value ($L = 1.8\ L_\odot$), lower than our determination ($L = 3.98\ L_\odot$). In general our result agrees with previous modeling attempts based on a "single-cavity" geometry. In particular, we find a good agreement for i, θ, $\dot{M}$, and R_c.

4.7. CoKu Tau 1

This source is located in the L1495 cloud. Strom & Strom (1994) obtained an M2e spectral type for this object. The central source is a binary star with a separation of ∼0.″24 (Padgett et al. 1999).

The SED of this object covers the 0.55–1300 μm spectral range with a peak around 70 μm and a slight decrease from 2 to 4 μm. The *Spitzer* spectrum shows an emission feature at 10 μm. Furlan et al. (2008) suggested that the shape of this emission is mainly generated by the envelope, while the disk only contributes with a weak absorption. NICMOS images reveal a faint binary central star with four filamentary reflection nebulae curving parabolically away from the central source. We analyze this object as a single target and present in Table 4 our best SED model derived from the grid of R06. In Table 5 and Figure 11, we show our combined (SED+images) model. In this analysis, we adopted the stellar temperature ($T_{star} = 4000$ K) previously determined by White & Hillenbrand (2004). Our combined model reproduces well the general shape of the SED, the mid-infrared spectrum and the NICMOS images. However, this model underestimates the fluxes for wavelengths longer than 100 μm. We suggest that long-wavelength part of the SED could be affected by dust emission in the surrounding cloud (Jayawardhana et al. 2001) or external illumination heating the outer envelope.

Parameters derived from Stark et al. (2006) and Furlan et al. (2008), as well as R06's grid model (see Table 4) and our combined model (see Table 5) are listed in Table 13. The inclusion of the *HST*/NICMOS images in our model attempt modified the inclination to the line of sight (i: 81.°3 versus 87.°1), the cavity opening angle (θ: 20° versus 39.°9), and the disk inner radius (R_{min}: 28.8 R_{star} versus 23.8 R_{star}).

Padgett et al. (1999) from *HST*/NICMOS images suggested an inclination angle (i) close to 90° and determined a cavity opening angle $\theta = 46.°0$. Andrews & Williams (2005) derived $M_{disk} = 0.002\ M_\odot$ from submillimeter data. From our modeling we derived $i = 81.3$, $\theta = 20.°0$, $M_{disk} = 0.003\ M_\odot$ in reasonable agreement with previous determinations. White & Hillenbrand

Table 13
Different Models for CoKu Tau 1

Parameter	Grid Model	Combined Model	Stark et al. (2006)	Furlan et al. (2008)
M_{star} ($M_\odot$)	1.27	0.70	0.50	
R_{star} ($R_\odot$)	4.15	3.50	2.50	2.00
T_{star} (K)	4380	4000	3800	
$\dot{M}$ ($M_\odot$ yr^{-1})	6.9×10^{-7}	1.4×10^{-7}	2.0×10^{-7}	
R_c (AU)	105.5	30.0	50.0	40.0
R_{min} (R_{star})	23.8	28.8	3.0	7.0
R_{max} (AU)	6180	3600	5000	5000
M_{env} ($M_\odot$)	0.02	0.003		
M_{disk} ($M_\odot$)	0.032	0.003	0.01	
$\dot{M}_{disk}$ ($M_\odot$ yr^{-1})	2.7×10^{-7}	2.4×10^{-8}		
A	2.009	2.176	2.250	
B	1.009	1.176	1.250	
θ(°)	39.9	20.0	20.0	5.0
i(°)	87.1	81.3	64.0	80.0
ρ_1(g cm^{-3})	3.3×10^{-15}	8.9×10^{-16}		5.0×10^{-15}
L_{tot}($L_\odot$)	7.60	1.91	0.30	1.10

Note. Symbols for model parameters are as indicated in Table 3.

(2004) derived a disk mass accretion rate, $\dot{M}_{acc} = 4.4 \times 10^{-8}\ M_\odot\ yr^{-1}$, similar to the value obtained from our combined model, $\dot{M}_{disk} = 2.4 \times 10^{-8}\ M_\odot\ yr^{-1}$.

Our centrifugal radius, R_c, agrees with previous determinations. In contrast, the value we derived for R_{min} (28.8 R_{star}) differs from the values adopted by Stark et al. (2006, $R_{min} = 3.0\ R_{star}$) and Furlan et al. (2008, $R_{min} = 7.0\ R_{star}$). In addition our determination for M_{disk} (0.003 $M_\odot$) is lower than Stark et al.'s (2006) estimate (0.01 $M_\odot$). These authors suggested that this source is near the end of the embedded phase or Class I stage of the evolution.

From our combined (SED+images) analysis, we obtained a disk accretion rate similar to that expected for Class I objects (Whitney et al. 2003a). However, the envelope accretion rate, the mass of disk, and the mass of envelope are relatively low for a Class I protostar. In particular, the low value for the mass of the envelope ($M_{env} = 0.003\ M_\odot$) suggests that CoKu Tau 1 may be an evolved Class I object. We derived a mass accretion, opening angle, and R_c that lie within the range of values given by Stark et al. (2006). However, our inclination angle is larger (∼81°) than that derived by these authors (64°) but agrees with Furlan et al.'s (2008) value (80°), suggesting that this is almost an edge-on source. Model SEDs with $i \sim 65°$ do not fit the fluxes in the infrared region. Our opening angle (20°) agrees with Stark et al.'s (2006) value (20°) but not with Furlan et al.'s (2008) determination (5°). If we reduce the opening angle we are not able to fit the near- and mid-infrared parts of the SED and the model image does not resemble the shape of the observed cavity.

4.8. DG Tau B

This star is not optically visible, has an infrared bipolar nebula (Stapelfeldt et al. 1997), and is associated with an optical and a large molecular jet (Mundt & Fried 1983; Mitchell et al. 1997). Hartmann et al. (2005) classified this object as a Class I–II transition star.

The *Spitzer* spectrum reveals a deep absorption feature at 10 μm. We caution that fluxes in Figures 12 and 13 and Table 2 for wavelengths longer than 36 μm are only upper limits. IRAS fluxes are not reliable due to the likely contamination from nearby DG Tau (located ∼ 1′ from DG Tau B). Submillimeter and millimeter data from Andrews & Williams (2005) belong to DG Tau. However, they are useful to our modeling attempt of DG Tau B as upper limits. The NICMOS images of DG Tau B show a bipolar reflection nebula with a V-shaped Eastern lobe and fainter Western lobe. The nebula is crossed by a dark lane; however, the central source is visible, probably due to the favorable orientation of the star with respect to the line of sight.

As with the rest of the sources, we list in Table 4 the initial SED model derived from the grid of models of R06. In Table 5 and Figures 12 and 13, we show two models for this source. Our first model reproduces the NICMOS images but fails to fit the SED, and in particular the IRS spectrum, between 13 and 36 μm (model a, Table 5, Figure 12). The second model fits the complete IRS spectrum from 5 to 36 μm but ignores the NICMOS images. This model, however, fails to fit fluxes for wavelengths shorter than 3 μm (model b, Table 5, Figure 13).

In this analysis, we initially considered two types of cavities: curved (or polynomial-shaped) and streamline (or conical, on large scales). For the rest of the analyzed sources, we chose curved cavities and were able to find good matches to both the SED and the images. In the case of DG Tau B, we adopted a streamline shape for the cavity because of the V-shape of the Eastern lobe. This forced us to modify the input set of parameters for the combined analyses (SED+images, SED without the NICMOS images) obtained from the grid of the R06 models, since the grid only considers curved cavities. The main difference is a lower envelope infall rate corresponding to the streamline shape cavity because the streamline cavity carves out less envelope mass in the inner regions (W03a).

Model a reproduces fairly well the SED (with the exception of the 12–36 μm region) and the NICMOS images. In addition, the model images reproduce the shape as well as the dark lane of the observed *HST* images. Model b, on the other hand, fits the SED for wavelengths longer than 3 μm but provides a poor approximation to the NICMOS images. We note that both models a and b match the deep absorption feature at 10 μm (see Figures 12 and 13).

Models a and b differ in their central source properties; in particular, we derive L_{tot} of 2.1 $L_\odot$ and 4 $L_\odot$, model a and b, respectively. In addition, the cavity opening angle (θ), the disk radial density (A), and scale height exponent (B) are

Table 14
Different Models for DG Tau B

Parameter	Grid Model	Model a[a]	Model b[b]	Stark et al. (2006)	Furlan et al. (2008)
M_{star} ($M_\odot$)	0.13	0.70	0.80	0.50	
R_{star} ($R_\odot$)	4.56	2.50	2.70	2.50	2.00
T_{star} (K)	2706	4000	4100	3800	
$\dot{M}$ ($M_\odot$ yr^{-1})	1.0×10^{-6}	8.0×10^{-6}	3.8×10^{-6}	5.0×10^{-6}	
R_c (AU)	2.3	300.0	100.0	300.0	60.0
R_{min} (R_{star})	1.0	14.4	12.2	3.0	1.0
R_{max} (AU)	1569	1157	1157	5000	10000
M_{env} ($M_\odot$)	0.11	0.03	0.03		
M_{disk} ($M_\odot$)	0.003	0.100	0.060	0.040	
$\dot{M}_{disk}$ ($M_\odot$ yr^{-1})	1.1×10^{-7}	5.0×10^{-7}	8.0×10^{-7}		
A	2.029	2.210	2.050	2.250	
B	1.029	1.210	1.050	1.250	
$\theta(^\circ)$	3.9	11.0	4.0	30.0	10.0
$i(^\circ)$	49.5	70.0	70.0	73.0	55.0
ρ_1(g cm^{-3})	1.5×10^{-14}	5.1×10^{-14}	2.3×10^{-14}		3.5×10^{-14}
L_{tot} ($L_\odot$)	1.81	2.10	4.00	0.20	2.50

Notes. Symbols for model parameters are as indicated in Table 3.
[a] Model a corresponds to the NICMOS images+SED, excluding the 12–36 μm region, (see Figure 12).
[b] Model b fits the SED, including the *Spitzer* spectrum, ignoring the NICMOS images (see Figure 13).

Table 15
Values of χ^2 Corresponding to the Grid of R06 and to Our Combined Best Model

Name	χ^2	
	R06 models	Combined Analysis[a]
IRAS 04016+2610	317	112
IRAS 04248+2612	168	181
IRAS 04302+2247	203	218
IRAS 04325+2402	234	107
IRAS 04361+2547	75	35[b]
IRAS 04361+2547		290[c]
IRAS 04368+2557	226	26
CoKu Tau 1	294	150
DG Tau B	206	256[d]
DG Tau B	206	269[e]

Notes.
[a] In this case, the χ^2 was calculated only for the SED, excluding IRS spectra, in the manner described by R06.
[b] IRAS 04361+2547, model a: value derived for the SED+images model.
[c] IRAS 04361+2547, model b: value derived for the *Spitzer* 5–36 μm spectrum model.
[d] DG Tau B, model a: value derived for the NICMOS images+SED, excluding the 12–36 μm region.
[e] DG Tau B, model b: value derived for the SED, including the IRS spectrum, but ignoring the NICMOS images.

different. On the other hand, we obtain the same values for the inclination angle (i), the envelope outer radius (R_{max}) and the mass of the envelope (M_{env}). We derive a disk mass (M_{disk}) of 0.10 and 0.06 $M_\odot$ (models a and b), a disk accretion rate ($\dot{M}_{disk} = 5 \times 10^{-7}\ M_\odot$ yr^{-1} and $8 \times 10^{-7}\ M_\odot$ yr^{-1}, models a and b), and a mass accretion rate for the envelope of ($\dot{M} = 8.0 \times 10^{-6}\ M_\odot$ yr^{-1} and $3.8 \times 10^{-6}\ M_\odot$ yr^{-1}, models a and b, respectively) all consistent with parameters for a Stage I (embedded, infalling envelope; R06; Robitaille et al. 2007) source, despite earlier SED classification as I/II transition object (Hartmann et al. 2005). We also note that M_{disk} and $\dot{M}_{disk}$ are among the highest in our sample.

In Table 14, we list different models from the literature (Stark et al. 2006; Furlan et al. 2008) for DG Tau B as well as R06's grid model (see Table 4) and our combined models (see Table 5). The modeling of the *HST*/NICMOS images (model a, see Table 14 and Figure 12) introduces modification in the inclination to the line of sight (i: 70° versus 49.°5), the cavity opening angle (θ: 11° versus 3.°9), and inner radius of the disk (R_{min}: 14.4 R_{star} versus 1.0 R_{star}).

From the *HST*/NICMOS images Padgett et al. (1999) suggested $i \sim 90°$ and derived different opening angles for the east and west lobes of the cavity, $\theta = 41.°5$ and $\theta = 22.°5$, respectively (see Figure 13, lower left panel). We derived $i = 70°$ for both our models a and b in reasonable agreement with Padgett et al.'s (1999) estimate. However for the cavity opening angle, we obtained $\theta = 11.°0$ for model a and $\theta = 4.°0$ for model b, in both cases smaller than Padgett et al.'s (1999).

As expected, in general model a agrees better with Stark et al.'s (2006) parameters and model b with Furlan et al.'s (2008) determinations (see Table 14). Stark et al. (2006) analyzed the *HST*/NICMOS images, while Furlan et al. (2008) fit the SED, including the IRS/*Spitzer* spectrum. We note that Furlan et al. (2008) did not obtain a good fit of the IRS spectrum for wavelengths longer than 20 μm. Our model has a higher inclination (70° versus 55°) and also a larger R_c (300–100 AU versus 60 AU) than Furlan et al.'s (2008). Our inclination angle is based on the NICMOS images and should be more reliable. If we adopt $R_c < 100$ AU and an inclination around the value derived by Furlan et al. (2008), the model SED appears to have a 10 μm absorption deeper than the observed feature, and the model images are more extended than the observed images. Finally, the stellar parameters (M_{star}, R_{star} and T_{star}) and the envelope accretion rate ($\dot{M}$) agree with those adopted or derived by other authors. We prefer model a because it fits the images better, and most of the SED.

5. SUMMARY AND CONCLUSIONS

In this paper, we present combined SED+images modeling of eight Taurus protostellar objects with Class I/II SEDs. We assembled the SEDs using the fluxes from the literature, used *Spitzer* spectral data obtained by Furlan et al. (2008), and *HST*/NICMOS and/or *Spitzer*/IRAC images from Padgett et al. (1999, 2005). We initially selected the best-fit SED from the grid of models developed by R06. We then used the code of W03b to find a model for each source that matches

all the data. In this manner, we analyzed SEDs in a wide spectral range (0.55–1300 μm), including 5–36 μm spectra, and high-resolution images in the near-infrared as well as IRAC mid-infrared data to derive reliable physical and geometrical parameters of the selected Taurus sources.

In Table 15, we show the χ^2 values corresponding to R06's best-fit SED and to the combined (SED+images) model for each source. In the latter case (the combined model), the χ^2 is calculated only for the corresponding SEDs, excluding the IRS spectra in the manner described by R06. For IRAS 04248+2612, IRAS 04302+2247, and DG Tau B, the χ^2 value from the R06 models fit is smaller than that obtained from the combined model. The contrary is true for the rest of the sources. In the case of the combined model, we were able to choose an arbitrary step for the different parameters whereas the R06 grid used fix values. Thus, a smaller χ^2 for the combined model in relation to the value derived from R06's grid may reflect this fact. We note that with the exception of IRAS 04368+2557, the χ^2's derived from the R06 models and from the combined analyses are of the same order of magnitude. However, the combined analyses provide much better constrained sets of parameters that match all available data, including high-resolution *HST* images. In other words, a relatively small χ^2 obtained from the R06 grid does not always guarantee model images that reproduce the observed images.

Table 4 shows the model parameters obtained by applying Robitaille et al.'s (2007) SED fits, and Table 5 shows those corresponding to the combined (SED+images) modeling. In general, values derived for each parameter in both analyses are significantly different. To derive a consistent set of parameters for each YSO, it is recommended to perform combined SED and image analyses that make use of all available data and better constrain physical and geometrical properties of the star+disk+envelope systems.

Images, in particular high-resolution near- and mid-infrared images, can provide information on the viewing angle, the extent, and shape of the disk as well as the size and shape of the outflow cavity (Stark et al. 2006). However, these images are not always available. In those cases, the SED modeling can be constrained by the availability of additional information on particular parameters. For example, the detection of outflows can provide some indications on the inclination to the line of sight (Hogerheijde et al. 1998), submillimeter and millimeter data can constrain the mass of the disk and of the envelope (Motte & André 2001; Shirley et al. 2000), spectra for the sources can be used to derive the temperatures of central stars (White & Hillenbrand 2004), etc. In this manner, SED modeling can produce more reliable set of parameters.

The near-infrared variability of the sources introduces an additional difficulty when trying to model the SEDs. Park & Kenyon (2002) detected brightness variations of ~0.1–0.5 mag in many Taurus Class I sources (see also Beck 2007). This effect is particularly significant for IRAS 04016+2610 and IRAS 04361+2547 (see Figures 2, 8, and 9) for which Park & Kenyon (2002) estimated brightness variations of 20% or more. For this reason, it would be desirable to model contemporaneous data, representing one single state of the protostar.

Table 1 lists SED luminosities from Kenyon & Hartmann (1995) calculated by integrating the SEDs. Our best model derived luminosities (see Table 5) are, in general, higher than luminosities in Table 1. Furlan et al. (2008) found the same trend in their sample. As discussed by W03a, the integrated SED varies with viewing angle, with edge-on sources having lower integrated fluxes than more pole-on. Thus, for edge-on sources, the true luminosity is higher than the integrated SED, and for pole-on sources, the true luminosity is lower than the integrated SED. For intermediate viewing angles, the true luminosity is close to the integrated SED. All of our modeled sources are estimated to be close to edge-on. The only exception corresponds to model a of IRAS 04361+2547 (see Table 5 and Figure 8). This model gives $i = 18.^\circ2$ and $L_{\rm tot} = 2.51\ L_\odot$. The integrated SED luminosity determined by Kenyon & Hartmann (1995) for this source is 2.9 $L_\odot$ (see Table 1). In this case, the model luminosity is lower than the integrated luminosity, as expected for a near pole-on source. In any event, as discussed in Section 4.5, we proposed model b (not model a) as our preferred model for this object.

It is interesting to note that our best models give relatively high inclination angles for the analyzed sources (see Table 5). Inclination angles close to edge-on make easier the detection of disks and envelopes by direct imaging, due to obscuration of the bright central starlight. Since we chose to model objects showing extended emission, it is not surprising that we are determining high inclinations for most of our sources.

Our stellar mass estimates should also improve over previous estimates due to the improved luminosity estimate, and using temperatures derived from stellar spectra (White & Hillenbrand 2004). However, we note that since several of these objects (5 out of 8) are binaries, our stellar mass estimates are all upper limits for the most massive source in the binary pair.

For IRAS 04248+2612 we determined the lowest stellar mass in our sample, ~0.07 $M_\odot$, in agreement with White & Hillenbrand (2004). Some of the selected Class I sources have more massive disks, larger disk mass accretion and A and B values than typical Class II sources (0.01 $M_\odot$, 2.25, 1.25, $2 \times 10^{-8}\ M_\odot\ {\rm yr}^{-1}$, respectively, W03b). This and their derived envelope accretion rates are consistent with the Stage I (embedded, infalling envelope; R06; Robitaille et al. 2007) assignment for all of these sources. For CoKu Tau 1 we obtained a very low value for the mass of the envelope ($\sim$0.003 $M_\odot$). The envelope accretion rate is lowest in our sample, $\dot{M} = 1.4 \times 10^{-7}\ M_\odot\ {\rm yr}^{-1}$ and lower than "typical" values for Class I objects (W03b). These facts suggest that CoKu Tau 1 is probably a more evolved Class I object.

In general, our combined models agree with previous published analyses. When we found a difference between these analyses and our parameters, we re-ran the models using published values. However, we were unable to find a good match to one or all of the components. In most of the cases, previous modeling was based on individual analyses of only the SED, the SED including the IRS spectrum, or the images. Our combined models should provide more reliable determinations of the physical and geometrical parameters.

We thank the referee of this paper for the detailed report as well as for suggestions that improved the content and presentation of our work. Support for this work was provided in part by NASA through the *Spitzer Space Telescope* Theoretical Research Programs, through a contract issued by the Jet Propulsion Laboratory, California Institute of Technology under a contract with NASA.

REFERENCES

Adams, F. C., Lada, C. J., & Shu, F. H. 1987, ApJ, 308, 788
Akeson, R. L., Ciardi, D. R., Van Belle, G. T., & Creech-Eakman, M. J. 2002, ApJ, 566, 1124

André, P., Ward-Thompson, D., & Barsony, M. 1993, ApJ, 406, 122
André, P., Ward-Thompson, D., & Barsony, M. 2000, in Protostars and Planets IV, ed. V. Mannings, A. P. Boss, & S. S. Russell (Tucson, AZ: Univ. Arizona Press), 59
Andrews, S. M., & Williams, J. P. 2005, ApJ, 631, 1134
Barsony, M., & Kenyon, S. J. 1992, ApJ, 384, 53
Beck, T. L. 2007, AJ, 133, 1673
Beichman, C. A. 1986, ApJ, 307, 337
Belloche, A., André, P., Despois, D., & Bilinder, S. 2002, A&A, 393, 947
Benson, P., & Meyers, P. C. 1989, ApJ, 71, 89
Bernasconi, P. A., & Meader, A. 1996, A&A, 307, 829
Bontemps, S., André, P., Terebey, S., & Cabrit, S. 1996, A&A, 311, 858
Brinch, C., Crapsi, A., Hogerheijde, M. R., & Jorgensen, J. K. 2007a, A&A, 461, 1037
Brinch, C., Crapsi, A., Jorgensen, J. K., Hogerheijde, M. R., & Hill, T. 2007b, A&A, 475, 915
Cassen, P., & Moosman, A. 1981, Icarus, 48, 353
Clark, F. O. 1991, ApJS, 75, 611
Cohen, M., & Schwartz, R. D. 1987, ApJ, 316, 311
Dent, W. R. F., Matthews, H. E., & Ward-Thompson, D. 1998, MNRAS, 301, 1049
Duchene, G., Bouvier, J., Bontemps, S., André, P., & Motte, F. 2004, A&A, 427, 651
Eisner, J. A., Hillebrand, L. A., Carpenter, J. M., & Wolf, S. 2005, ApJ, 635, 396
Fuller, G. A., Ladd, E. F., & Hodapp, K.-W. 1996, ApJ, 463, 97
Furlan, E., et al. 2008, ApJS, 176, 184
Gómez, M., Whitney, B. A., & Kenyon, S. J. 1997, AJ, 114, 1138
Gramajo, L. V., Whitney, B. A., Kenyon, S. J., Gómez, M., & Merrill, K. M. 2007, AJ, 133, 1911
Hartmann, L., Boss, A., Calvet, N., & Whitney, B. 1994, ApJ, 430, L49
Hartmann, L., Calvet, N., Allen, L., Chen, H., & Jayawardhana, R. 1999, AJ, 118, 1784
Hartmann, L., Calvet, N., & Boss, A. 1996, ApJ, 464, 387
Hartmann, L., Megeath, S. T., Allen, L., Luhman, K., Calvet, N., D'Alessio, P., Franco-Hernández, R., & Fazio, G. 2005, ApJ, 629, 896
Hogerheijde, M. R., & Sandell, G. 2000, ApJ, 534, 880
Hogerheijde, M. R., van Dishoeck, E. F., Blake, G. A., & van Langevelde, H. J. 1998, ApJ, 502, 315
Jayawardhana, R., Hartmann, L., & Calvet, N. 2001, ApJ, 548, 310
Kenyon, S. J., Calvet, N., & Hartmann, L. 1993a, ApJ, 414, 676
Kenyon, S. J., Gómez, M., Marzke, R. O., & Hartmann, L. 1994, AJ, 108, 251
Kenyon, S. J., & Hartmann, L. 1995, ApJS, 101, 117
Kenyon, S. J., Whitney, B. A., Gómez, M., & Hartmann, L. 1993b, ApJ, 414, 773
Kessler-Silacci, J. E., et al. 2004, BAAS, 37, 378
Lada, C. J. 1987, in Star-forming Regions, ed. M. Peimbert & J. Jugaka (Dordrecht: Kluwer), 1
Lada, C. J., & Wilking, B. A. 1984, ApJ, 287, 610
Loinard, L., Rodríguez, L. F., D'Alessio, P., Wilner, D. J., & Ho, P. T. P. 2002, ApJ, 581, 109
Lucas, P. W., & Roche, P. F. 1997, MNRAS, 286, 895
Mitchell, G. F., Sargent, A. I., & Mannings, V. 1997, ApJ, 483, 127
Moriarty-Schienven, G. H., Wannier, P. G., Keene, J., & Tamura, M. 1994, ApJ, 436, 800
Moriarty-Schienven, G. H., Wannier, P. G., Tamura, M., & Keene, J. 1992, ApJ, 400, 260
Motte, F., & André, P. 2001, A&A, 365, 440
Mundt, R., & Fried, J. 1983, ApJ, 274, L83
Myers, P. C., Fuller, G. A., Mathieu, R. D., Beichman, C. A., Benson, P. J., Schild, R. E., & Emerson, J. P. 1987, ApJ, 319, 34
Ohashi, N., Hayashi, M., Kawabw, R., & Ishiguro, M. 1996, ApJ, 466, 317
Padgett, D. L., Brandner, W., Stapelfeldt, K. R., Strom, S. E., Terebey, S., & Koermer, D. 1999, AJ, 117, 1490
Padgett, D. L., et al. 2005, BAAS, 39, 750
Padoan, P., Cambrésy, L., & Langer, W. 2002, ApJ, 580, L57
Park, S., & Kenyon, S. J. 2002, AJ, 123, 3370
Pontoppidan, K. M., Dartois, E., van Dishoeck, E. F., Thi, W.-F., & d'Hendecourt, L. 2003, A&A, 404, L17
Robitaille, T. P., Whitney, B. A., Indebetouw, R., & Wood, K. 2007, ApJS, 169, 328
Robitaille, T. P., Whitney, B. A., Indebetouw, R., Wood, K., & Denzmore, P. 2006, ApJS, 167, 256 (R06)
Sarceno, P., André, P., Ceccarelli, C., Griffin, M., & Molinari, S. 1996, A&A, 309, 827
Siess, L., Dufour, E., & Forestini, M. 2000, A&A, 358, 593
Shirley, Y. L., Evans, N. J. II., Rawlings, J. M. C., & Gregersen, E. M. 2000, ApJS, 131, 249
Stapelfeldt, K. M., Burrows, C. J., & Krist, J. E., and WFPC2 Science Team 1997, in IAU Symp. 182, Herbig-Haro Flows and the Birth of Stars, ed. B. Reipurth & C. Bertout (Dordrecht: Kluwer), 355
Stark, D. P., Whitney, B. A., Stassun, K., & Wood, K. 2006, ApJ, 649, 900
Strom, K. M., & Strom, S. E. 1994, ApJ, 424, 237
Tafalla, M., Santiago, J., Johnstone, D., & Bachiller, R. 2004, A&A, 423, 21
Tamura, M., Gatley, I., Joyce, R. R., Ueno, M., Suto, H., & Sekiguchi, M. 1991, ApJ, 378, 611
Terebey, S., Beichman, C. A., Gautier, T. N., & Hester, J. J. 1990, ApJ, 362, L63
Terebey, S., Van Buren, D., Matthews, K., & Padgett, D. L. 2000, AJ, 119, 2341
Tobin, J. J., Hartmann, L., Calvet, N., & D'Alessio, P. 2008, ApJ, 679, 1364
Watson, D. M., et al. 2004, ApJS, 154, 391
Weaver, W. B., & Jones, G. 1992, ApJS, 78, 239
White, R. J., & Hillenbrand, L. A. 2004, ApJ, 616, 998
Whitney, B. A., & Hartmann, L. 1993, ApJ, 402, 605
Whitney, B. A., Kenyon, S. J., & Gómez, M. 1997, ApJ, 485, 703
Whitney, B. A., & Wolff, M. J. 2002, ApJ, 574, 205
Whitney, B. A., Wood, K., Bjorkman, J. E., & Cohen, M. 2003a, ApJ, 598, 1099 (W03a)
Whitney, B. A., Wood, K., Bjorkman, J. E., & Wolff, M. J. 2003b, ApJ, 591, 1049 (W03b)
Wolf, S., & Henning, T. 2000, Comput. Phys. Commun., 132, 166
Wolf, S., Padgett, D. L., & Stapelfeldt, K. R. 2003, ApJ, 588, 373
Wolf, S., Schegerer, A., Beuther, H., Padgett, D. L., & Stapelfeldt, K. R. 2008, ApJ, 674, 101
Wood, K., Smith, D., Whitney, B., Stassun, K., Kenyon, S. J., Wolff, M. J., & Bjorkman, K. S. 2001, ApJ, 561, 299
Young, C. H., Shirley, Y. L., & Evans, N. J., II. 2003, ApJS, 145, 111